



# An Innovative Hybrid SG-CEEMDAN-ARIMA-LSTM Model for Forecasting Meteorological Drought: Trends and Forecasting

Siphamandla Sibiya<sup>1,3</sup>, Nkanyiso Mbatha<sup>2</sup>, Shaun Ramroop<sup>1</sup>, Sileshi Melesse<sup>1</sup>

5 <sup>1</sup>School of Mathematics, Statistics, and Computer Science, University of KwaZulu-Natal, Pietermaritzburg Campus, Private Bag X01, Scottsville 32009, South Africa.

<sup>2</sup>Council for Scientific and Industrial Research, Holistic Climate Change, Smart Places, Mering Naude Road, Brummeria, Pretoria 0001, South Africa.

<sup>3</sup>Department of Mathematical Sciences, University of Zululand, Private Bag X1001, KwaDlangezwa 3886, South Africa.

10 *Correspondence to:* Siphamandla Sibiya (Siphasibiya@gmail.com)

**Abstract.** Droughts are defined as extended periods of below-average rainfall resulting in a shortage of water and have significant impacts on ecosystems, agriculture, and water supplies. One of the most challenging aspects of addressing drought is trend patterns and developing accurate prediction models that will be crucial for efficient mitigation and resource management. Analyzing drought is inherently uncertain and complex due to the dynamic and evolving character of climate

15 trends. This study used a special method called the modified Mann-Kendall (MMK) approach and a new trend analysis (ITA) to find trends and introduced a better way to make predictions by using the Standardized Precipitation Index (SPI) along with a combined model that takes advantage of the Savitzky-Golay filter and Complete Ensemble Empirical Mode Decomposition

20 with Adaptive Noise (SG-CEEMDAN) for preparation, plus Autoregressive Integrated Moving Average (ARIMA) and Long Short-Term Memory (LSTM) techniques. In terms of trend analysis of the SPIs, MK and MMK tests revealed a most statistically significant decreasing trend. For example, Pongolapoort Dam showed negative Z-score (p-values) for the SPI-6, SPI-9, and SPI-12 in the MK and MMK tests, which are represented as  $(-7.19 (6.12e^{-13}), -8.74 (< 0.00), -9.83 (< 0.00)$  and  $-8.22 (2.22e^{-16}), -5.44 (5.40e^{-8}), -6.51 (7.41e^{-11})$ , respectively. Additionally, the ITA confirmed a significant downward trend across all time scales of the SPI. The SPI forecasting results show that the hybrid model, called SG-

25 CEEMDAN-ARIMA-LSTM, had the best prediction accuracy compared to all other models for every SPI time scale. The coefficient of determination ( $R^2$ ) values of the proposed hybrid model was notably high: 0.9839 for SPI-6, 0.9892 for SPI-9, and 0.9990 for SPI-12. This demonstrates that the hybrid model offers the best fit to the data and is the most suitable choice

for forecasting short-to-long-term drought conditions in the uMkhanyakude district. Furthermore, the inclusion of decomposition techniques, such as SG, CEEMDAN, and SG-CEEMDAN, significantly enhances the performance of the model.



## 1. Introduction

35 Drought is an extended hydrometeorological phenomenon that affects large areas and inflicts considerable harm (Bagmar and Khudri, 2021; Kalisa et al., 2021; Song and Park, 2023). Drought is among the most devastating natural phenomena due to its extensive and enduring impacts (Marengo et al., 2017; Jahanzaib et al., 2021; Dikshit et al., 2022; Gavahi et al., 2022). Drought emerged from climate change, resulting in elevated global temperatures and less precipitation (Chen et al., 2024). Prolonged exceptionally low precipitation leads to water scarcity and can cause soil moisture deficiency, hence significantly jeopardizing food security (Wang et al., 2023). Drought, a frequent and intricate climatic occurrence, has historically had adverse consequences on economic, environmental, and social sectors, negatively impacting civilization (Hinge et al., 2022; Xu et al., 2022). Drought is defined as extended water deficiency that adversely affects edaphic, hydrological, meteorological, and social elements (Wilhite and Glantz, 1985; Cunha et al., 2019; Adeola et al., 2021; Shang et al., 2023). The occurrence of droughts is acknowledged as a critical factor in water resources planning and management (Bagmar and Khudri, 2021). Drought is a 40 physical phenomenon and environmental hazard that can lead to catastrophe if reaction skills and vulnerability are insufficient to alleviate its effects (Ruwanza et al., 2022).

In response to global apprehension regarding climate change and its impact on local climates, there has been a heightened focus on analyzing trends in severe drought occurrences in recent years. Several studies have made significant contributions to this area of research, such as the investigations conducted by Labudová et al. (2017), Shiru et al. (2018), Polong et al. (2019), 45 Danandeh Mehr et al. (2019), Katipoğlu et al. (2022), Phuong et al. (2022), and Gond et al. (2023). Abarghouei et al. (2011) conducted a study in Iran to analyze the linear trends of Standardized Precipitation Index (SPI) indices at 3, 6, 9, 12, and 18-month intervals over a span of 30 years. The study determined that the level of drought in the country is escalating. Caloiero et al. (2018) utilized the Mann-Kendall and ISM techniques to examine potential developments in SPI across New Zealand. They identified both upward and downward trends in various places. In a similar manner, Jin et al. (2020) employed the Mann-Kendall and ISM techniques to analyze the trends in SPEI series at Zoige Wetland, China. Their findings indicated a prevalent 50 pattern of drying in most of the studied regions. Mehr and Vaheddoost (2020) conducted a study in Ankara Province, Turkey, using the well-known Spearman rank-order correlation coefficient, Sen's method, and trend analysis to look at the trends in SPI and SPEI over 3-, 6-, and 12-month periods. The findings revealed that the province had five instances of severe drought between 1971 and 2016. There were some discrepancies in the timing of these drought occurrences when comparing the 55 Standardized Precipitation Index (SPI) and the Standardized Precipitation Evapotranspiration Index (SPEI), especially when considering the 6- and 12-month periods. Although the observed drought events displayed a modest decrease in SPEI, the SPI did not demonstrate the same trend. Di Nunno et al. (2024) utilized the seasonal Mann-Kendall test and the Bayesian Changepoint Detection and Time Series Decomposition algorithm to assess the general trends for each cluster and SPI time scale. Additionally, they used these methods to detect sudden changes in trend and seasonality along the SPI time series, 60 respectively. The findings of the seasonal Mann-Kendall (MK) test indicated statistically significant upward trends in the SPI for all clusters, except for the southeastern region of the United Kingdom, where downward trends were seen, although they 65



were not statistically significant. Following the abovementioned trend analysis in drought studies, drought forecasts are important for enhancing the understanding of drought dynamics. Drought forecasting plays a key role in providing early drought warnings to mitigate its impacts and improve drought management (Balti et al., 2020; Zhang et al., 2022; Tan et al., 70 Zhang et al., 2024).

New and combined/hybrid models have become the main way to predict droughts, effectively handling the complex and changing nature of rainfall data. Consequently, hybrid models are extensively employed in drought research to enhance predictive accuracy. Alquraish et al. (2021) investigated the efficacy of three hybrid models: the Hidden Markov Model-Genetic Algorithm (HMM-GA), ARIMA-Genetic Algorithm (ARIMA-GA), and ARIMA-Genetic Algorithm-Artificial 75 Neural Network (ARIMA-GA-ANN), comparing them against the benchmarks of HMM and ARIMA for forecasting the Standardized Precipitation Index (SPI) in the Arabian Peninsula. The findings indicated that the hybrid models outperformed the benchmarked standalone model. Ding et al. (2022) employed a hybrid model integrating complementary ensemble empirical mode decomposition (CEEMD) and long short-term memory (LSTM) for predicting the standardized precipitation index (SPI) over various timescales in the Xinjiang Uygur Autonomous Region of China. The findings indicate that as the 80 timescale increases, the predictive accuracy of the LSTM and CEEMD-LSTM models progressively enhances. Xu et al. (2022) employed a hybrid model integrating CEEMD and ARIMA for the prediction of SPI across various timescales in the Ningxia Hui Autonomous Region. The results indicate that the CEEMD-ARIMA model exhibited strong concordance with the SPI values, demonstrating that the combined model surpassed the performance of the individual model. Latifoglu and Ozger (2023) 85 created a new method that combines phase transfer entropy (pTE) with the Tunable Q Factor Wavelet Transform (TQWT), which is improved using the Grey Wolf Optimization (GWO) algorithm. The subband data obtained from the SPI are assessed using Artificial Neural Networks (ANN), Support Vector Regression (SVR), Maximum Likelihood (ML), and the Gaussian Process Regression Model (GPR). The findings illustrate the enhanced efficacy of the pTE-GWO-TQWT-ML models compared to alternative approaches. The pTE-GWO-TQWT-GPR model exhibits superior predictive performance compared to the pTE-GWO-TQWT-ANN and pTE-GWO-TQWT-SVR models. Sibya et al. (2024) used a combined model that merges 90 CEEMDAN with ARIMA, LSTM, and ARIMA-LSTM methods to predict the Standardized Precipitation Index (SPI) at various time periods (SPI-6, SPI-9, and SPI-12) for Cape Town International Airport. The results indicated a significant alignment between the CEEMDAN-ARIMA-LSTM model and the SPI values, implying that the suggested hybrid model outperformed all other models. The aforementioned studies demonstrated the efficacy and adaptability of tailored hybrid models to meet diverse research objectives and enhance forecasting performance. A researcher must comprehend the strengths 95 and weaknesses of each model to develop a viable hybrid-based model (Tan et al. 2023). Therefore, using hybrid-based models is suggested because they have become a popular choice for researchers looking for new ways to create very reliable drought forecasting models.

Numerous researchers have developed extensive drought prediction models for the purpose of monitoring drought conditions.

100 These models are associated with some challenges when applying preprocessing techniques in conjunction with predictive



models (Sibya et al. 2024). Methods like decomposition techniques (such as EMD, EEMD, CEEMD, CEEMDAN, and VMD) and wavelet transformation require a lot of computer power, especially when working with large amounts of data or in real-time situations. To address these challenges, this study employed the Savitzky-Golay Filter in combination with CEEMDAN for data preprocessing. CEEMDAN can be easily affected by noise and often creates misleading Intrinsic Mode Functions (IMFs) when used directly on raw data, particularly in unstable time series like drought indices. By smoothing the data first with the Savitzky-Golay Filter, we reduce unnecessary high-frequency noise, which helps CEEMDAN create fewer IMFs and need fewer repetitions. This approach results in a reduced computational burden and yields better-separated intrinsic components. The application of the Savitzky-Golay filter enhances signal quality prior to decomposition, ensuring that meaningful components are retained. A smoother input resulting from Savitzky-Golay filtering facilitates quicker convergence, subsequently decreasing runtime and memory usage. With reduced noise and clearer IMFs, ARIMA and LSTM models are trained on more informative and stable inputs. This reduces the chance of the models getting confused by noisy data and helps them better understand real patterns in drought behavior, which leads to stronger and more reliable forecasting results. This paper discusses the novel hybrid model used for drought prediction.

The current scenario entails trend analysis to evaluate the trend pattern prior to forecasting the SPI series. The modified Mann-Kendall method and advanced trend analysis were utilized to examine the drought in the uMkhanyakude district. We identified change points in the SPI time series at intervals of 6, 9, and 12 months. We subsequently examined the SPI trend using a predictive modelling approach. The suggested methodology integrates the advantages of the Savitzky-Golay filter and Complete Ensemble Empirical Mode Decomposition with Adaptive Noise (SG-CEEMDAN) alongside Autoregressive Integrated Moving Average (ARIMA) and Long Short-Term Memory (LSTM) models for the prediction of drought occurrences. Using the SPI index trend analysis and prediction together is a combined approach that enhances our understanding of how droughts work. We selected the SPI as the drought index due to its simplicity and adaptability. It solely necessitates precipitation data for calculation, rendering it attainable in areas with scarce meteorological information. Its adaptability to diverse temporal scales facilitates a thorough evaluation of drought severity across varying durations. Nonetheless, the SPI has constraints as it relies exclusively on precipitation and neglects variables such as temperature and soil moisture, which are incorporated in more sophisticated indices like SPEI.

To the authors' knowledge, no prior research has investigated the changes in drought patterns related to trends and forecasted droughts using the predictive hybrid model SG-CEEMDAN-ARIMA-LSTM. Consequently, this model has not been introduced in the literature yet, even for alternative hydrometeorological applications. This paper enhances the evolving domain of climate modeling and drought prediction by introducing a novel hybrid forecasting method, clarifying its constraints, and suggesting potential directions for future improvements. The results derived from this study were meticulously analysed to provide valuable insights for: (1) the management of water resources to facilitate planning for water allocation and the implementation of adaptive strategies to alleviate drought impacts; (2) the design of infrastructure projects, including



reservoirs, irrigation systems, and water distribution networks, to accommodate evolving hydrological patterns; (3) the establishment of early warning systems for authorities to notify affected regions, thereby enabling prompt responses and  
135 preventive measures; (4) the enhancement of knowledge through the development of hybrid models for forecasting SPI-6, SPI-9, and SPI-12; and (5) the identification of optimal models for meteorological drought forecasting in semi-arid regions.<sup>2</sup>

## Material Methods

### 2.1. The Study Area

This study employed monthly precipitation records from 1980 to 2023, obtained from the South African Weather Service  
140 (SAWS) for the uMkhanyakude District in South Africa. The uMkhanyakude District Municipality is located in the far northern region of the KwaZulu-Natal (KZN) province (coordinates: 32.014489° S, 27.622242° E). The municipality covers a total area of 13,855 km<sup>2</sup>, making it the second largest in the province, exceeded only by the Zululand Municipality. The uMkhanyakude District was formed immediately after the local government elections in December 2000 as part of municipal demarcation, encompassing some of the most destitute and underdeveloped areas of KwaZulu-Natal. The uMkhanyakude District consists  
145 of four local municipalities: uMhlabuyalingana, Jozini, Big Five Hlabisa, and Mtubatuba. The municipality is geographically surrounded by Mozambique to the north, the Indian Ocean to the east, the uThungulu River to the south, Zululand to the west, and the Kingdom of Swaziland to the northwest. Figure 1 depicts the spatial arrangement of the stations, superimposed on the National Aeronautics and Space Administration (NASA) Shuttle Radar Topography Mission (SRTM) digital elevation model of the research area (Farr et al., 2007). The stations are situated in a relatively low-lying region in the eastern section of South  
150 Africa.

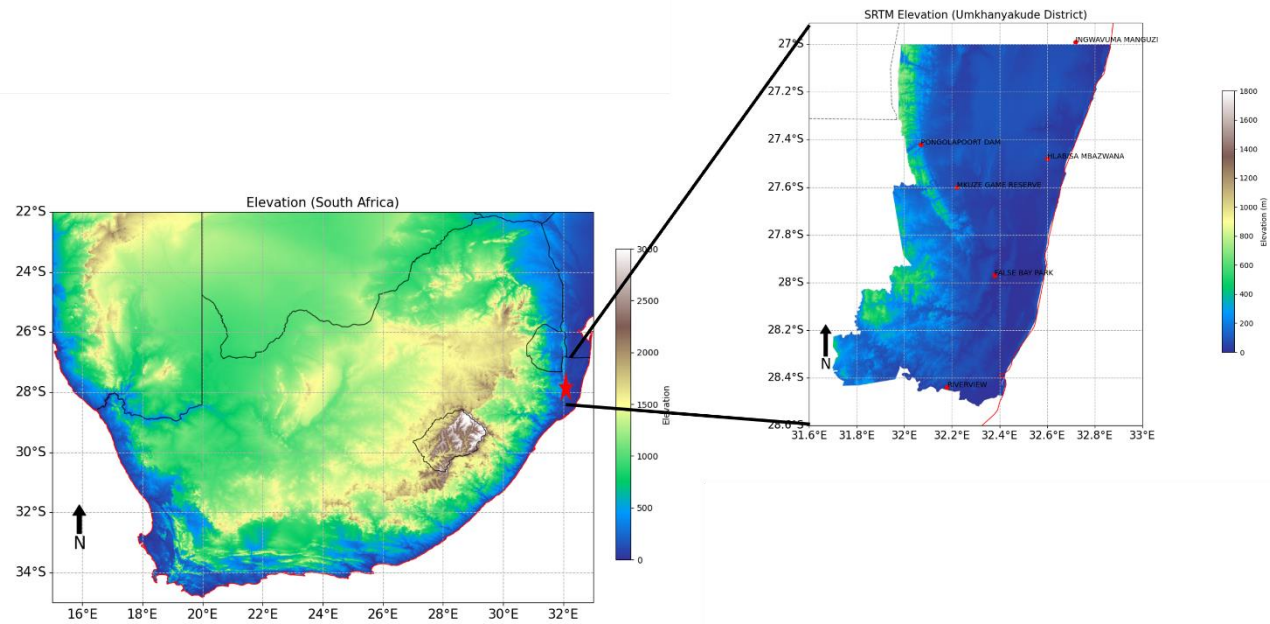


**Figure 1: Overview of the uMkhanyakude District (meteorological stations).**

## 155 2.2. Modified Mann-Kendall

The modified Mann-Kendall methodology derives from the nonparametric Mann-Kendall method (Mann, 1945; Kendall, 1975), which is extensively employed to detect trends in hydro-meteorological time series (Caloiero et al., 2011; Bard et al., 2015; Wang et al., 2017; Mirabbasi et al., 2020). The modified Mann-Kendall (MMK) test was employed for serially correlated data exhibiting a substantial lag-1 autocorrelation coefficient, utilising the variance correction method proposed by Yue et al. 160 (2002). Hamed and Rao (1998) created this methodology to eradicate all substantial autocorrelation in the time series. Under the assumption that the data are independent and identically distributed, the S statistic of the Mann-Kendall test is computed as follows (Sharifi et al. 2024):

$$S = \sum_{i=1}^{n-1} \sum_{j=i+1}^n \text{Sign}(x_j - x_i) \quad (1)$$



165 where  $n$  denote the sample size;  $x_i$  and  $x_j$  denote sequential  $i^{th}$  and  $j^{th}$  data points, respectively, and  $\text{sign}(\cdot)$  is the sign function which can be computed as

$$\text{Sign}(x_j - x_i) = \begin{cases} 1, & \text{if } x_j - x_i > 0 \\ 0, & \text{if } x_j - x_i = 0 \\ -1, & \text{if } x_j - x_i < 0 \end{cases} \quad (2)$$

with the mean and variance of the  $S$  statistics in equation are as follows (Helsel and Hirsch 1993; Ma et al. 2014; Ashraf et al. 2023)

$$E(S) = 0 \quad (3)$$

$$\text{Var}(S) = \frac{n(n-1)(2n+5) - \sum_{i=1}^p t_i(t_i-1)(2t_i+5)}{18} \quad (4)$$

170

where  $p$  is the number of tied groups and  $t_i$  denotes the number of data points in the  $t^{th}$  group. The second term represents an adjustment for tied group or censored data. The standardized Z statistic is calculated as

$$Z_{MK} = \begin{cases} \frac{S-1}{\sqrt{\text{Var}(S)}}, & S > 0 \\ 0, & S = 0 \\ \frac{S+1}{\sqrt{\text{Var}(S)}}, & S < 0 \end{cases} \quad (5)$$

The test statistic  $Z$  is used to measure the significance of the trends. In the modified Mann-Kendall approach, a modified variance of  $S$  is computed as follows (Hamed and Rao, 1998)

$$\text{Var}(S^*) = \text{Var}(S) \cdot \frac{n}{n^*} \quad (6)$$

175 where  $n^*$  is the effective sample size. The  $\frac{n}{n^*}$  ratio can be calculated as follows (Hamed and Rao, 1998)

$$\frac{n}{n^*} = 1 + \frac{2}{n(n-1)(n-2)} \sum_{i=1}^n (n-i)(n-i-1)(n-i-2)r_i \quad (7)$$

where  $r_i$  denotes the lag- $i$  significant autocorrelation coefficient of rank  $i$  in a time series. Then the standardized statistic of the  $S$  statistic, denoted as  $Z$ , can be derived as

$$Z_{MMK} = \begin{cases} \frac{S-1}{\sqrt{\text{Var}(S^*)}}, & S > 0 \\ 0, & S = 0 \\ \frac{S+1}{\sqrt{\text{Var}(S^*)}}, & S < 0 \end{cases} \quad (8)$$



180 If the calculated Z values ( $Z_{MK}$  and  $Z_{MMK}$ ) exceed the critical values of  $-Z_{1-\alpha/2}$  or fall below  $Z_{1-\alpha/2}$ , there is no discernible trend in the time series at the significance level of  $\alpha$ . If the Z value is positive and exceeds  $Z_{1-\alpha/2}$ , the trend is upward; conversely, if the Z value is negative and falls below  $-Z_{1-\alpha/2}$ , the trend is downward.

### 2.3. Innovative Trend Analysis

185 The Innovative Trend Analysis (ITA) method, initially introduced by Sen (2012), has been widely employed for detecting patterns in precipitation time series. Since its debut, the ITA technique has experienced substantial improvements in both mathematical and graphical aspects, as evidenced by Şen (2017) and Alashan (2018). The ITA method does not depend on assumptions of serial autocorrelation, normalcy, or record length, making it appropriate for both graphical and statistical trend analysis (Besha et al., 2022). Initially, the time series is bifurcated into two equal segments and organised in ascending order.

190 The initial segment of the time series ( $x_i: i = 1, 2, \dots, n/2$ ) is positioned along the horizontal x-axis, while the subsequent segment ( $x_j: j = n/2 + 1, n/2 + 2, \dots, n$ ) is situated along the vertical y-axis in the Cartesian coordinate system (Ashraf et al. 2023). The ITA approach visually represents trend analysis, specifically indicating monotonic growing, declining, and trendless circumstances (Oztopal and Şen, 2017; Likinaw et al., 2023). A monotonically growing or declining trend can be identified when the majority of points are situated above or below the  $45^\circ$  (1:1 line), respectively. A trendless condition arises 195 when the data points are clustered along the  $45^\circ$  line (Şen, 2012). We employ the magnitude of the slope parameter to convey information about monotonicity. The slope parameter of the ITA technique is a stochastic property dependent on the sample means of the first half ( $n_1$ ) and the second half ( $n_2$ ) of the time-series mean data values. According to Şen (2017), the straight-line trend slope ( $S_{ITA}$ ) can be estimated using the following expression:

$$S_{ITA} = \frac{2x(x_j - x_i)}{n} \quad (9)$$

where  $n$  represents the total number of observations,  $x_i$  and  $x_j$  are the arithmetic means of the first and second halves of the 200 sub-series, respectively. Given that  $x_i$  and  $x_j$  are stochastic variables, the expected value of the slope can be determined by analysing the expectancies of both the first and second halves of the time series (Alashan, 2020; Harka et al., 2021):

$$E(S_{ITA}) = \frac{2}{n} [E(x_j) - E(x_i)] \quad (10)$$

For the no trend condition,  $E(x_j) = E(x_i)$ , the  $E(S_{ITA}) = 0$  and standard deviation (SD) of the two half time-series ( $\sigma_{x_j} = \sigma_{x_i} = \sigma/\sqrt{n}$ ),  $\sigma$  is the SD of the parent series. If  $E(x_j) \neq E(x_i)$ , the differences between  $E(x_j)$  and  $E(x_i)$  gives the variance

$$\sigma_{S_{ITA}}^2 = \frac{8}{n^2} [E(x_j) - E(x_i)] \quad (11)$$

205 and the SD of the slope



$$\sigma_{S_{ITA}} = \frac{2\sqrt{2}}{n\sqrt{n}} \sigma \sqrt{1 - \rho_{x_j x_i}} \quad (12)$$

In the stochastic processes, the term  $\rho_{x_j x_i}$  is the correlation coefficient between the two mean values, and can be estimated as

$$\rho_{x_j x_i} = \frac{E(x_j x_i) - E(x_j)E(x_i)}{\sigma_{x_j} \sigma_{x_i}} \quad (13)$$

In the end, the upper and lower confidence limit (CL) of the trend slope was calculated (Şen 2017):

$$CL_{(1-\alpha)} = 0 \pm (Z_{1-\alpha/2}) \sigma_{S_{ITA}} \quad (14)$$

$Z_{1-\alpha/2}$  denotes the crucial slope for standardised time-series at  $\pm 1.96$  for a 95% significance level or  $\pm 1.645$  for a 90% significance level (Alashan, 2020). If the ITA slope value is beyond the lower and upper confidence limits, the null hypothesis of no significant trend should be rejected at the  $\alpha$  significance level (Şen, 2017). In a two-tailed scenario, the null hypothesis ( $H_0$ ) posits the absence of a trend in time-series data, while the alternative hypothesis ( $H_1$ ) asserts the presence of a trend in time-series data at a significance level of  $\alpha$ . If the slope,  $\pm S_{ITA} > \pm CL_{(1-\alpha)}$ , then ( $H_0$ ) is discarded in favour of ( $H_1$ ). The positive and negative values of  $S_{ITA}$  signify an upward and downward trend in the time-series data, respectively (Şen, 2017).

## 215 2.4. The SPI Calculation

For the purpose of analysing the severity of drought which is caused by a lack of water supply as a result of reduced precipitation in response to rising demand, the SPI was designed by McKee et al. (1993) and is based on probability (Zuo, 2021). Based on the cumulative likelihood of a specific amount of precipitation, the SPI indicator is calculated by fitting the precipitation throughout the same period with a certain distribution function. At its largest point, the SPI index represents the quantile of a normal distribution. Each time axis has an estimated drought index for 6, 9, and 12 months. This is based on the gamma probability density function, which considers the periodic distribution of precipitation for the corresponding data point. The expression of the density function for this distribution is as follow.

$$g(x) = \frac{1}{\beta^\alpha \Gamma(\alpha)} x^{\alpha-1} e^{-\frac{x}{\beta}} \quad (15)$$

where  $\alpha$  is the shape parameter,  $\beta$  is the scale parameter and  $x$  is the precipitation amount, and  $\Gamma(\alpha) = \int_0^\infty y^{\alpha-1} e^{-y} dy$  is gamma function. The maximum likelihood estimates of the parameters  $\alpha$  and  $\beta$  are:

$$\alpha = \frac{1}{4A} \left( 1 + \sqrt{1 + \frac{4A}{3}} \right) \quad (16)$$

225

$$\beta = \frac{\bar{x}}{n} \quad (17)$$



where  $A = \ln(\bar{x}) - \frac{\sum \ln(x)}{n}$ ,  $\bar{x}$  is the precipitation average and  $n$  is the sample size. The following equation applies the acquired parameters to the cumulative probability distribution:

$$G(x) = \int_0^x g(x)dx = \frac{1}{\beta^\alpha \Gamma(\alpha)} \int_0^x x^{\alpha-1} e^{-\frac{x}{\beta}} dx \quad (18)$$

230 G(x) represents the likelihood that the precipitation will be equal to or less than x. The distribution function for precipitation needs to be adjusted because the real precipitation samples can contain a value of 0. Based on this, we can calculate the cumulative probability as:

$$H(x) = q + (1 - q)G(x) \quad (19)$$

where q denotes the probability when precipitation equals zero. The probability of no rainfall, q, can be articulated as  $q = m/r$ , where m represents the number of days without rainfall and r denotes the number of days with rainfall (Song and Park, 2021).

235 Consequently, H(x) is converted to the conventional random variable Z of the standard normal distribution, characterised by a mean of 0 and a variance of 1, resulting in:

$$SPI = Z = \begin{cases} -\left(k - \frac{c_0 + c_1 k + c_2 k^2}{1 + d_1 k + d_2 k^2 + d_3 k^3}\right), & 0 < H(x) \leq 0.5 \\ +\left(k - \frac{c_0 + c_1 k + c_2 k^2}{1 + d_1 k + d_2 k^2 + d_3 k^3}\right), & 0.5 < H(x) \leq 1.0 \end{cases} \quad (20)$$

$$k = \begin{cases} \sqrt{\ln\left(\left(\frac{1}{H(x)}\right)^2\right)}, & 0 < H(x) \leq 0.5 \\ \sqrt{\ln\left(\left(\frac{1}{1-H(x)}\right)^2\right)}, & 0.5 < H(x) \leq 1.0 \end{cases} \quad (21)$$

where  $c_0 = 2,515517$ ,  $c_1 = 0.802853$ ,  $c_2 = 0,010328$ ,  $d_1 = 1,432788$ ,  $d_2 = 0,189269$ ,  $d_3 = 0,001308$  are constants. Furthermore, the SPI indicator is a standardised normalised index, establishing a correlational relationship with likelihood.

240 Table 1 presents the probability associated with each category of drought.

**Table 1. Drought classification using SPI values and corresponding event probability (Llyod-Hughes and Sanders 2002).**



SPI Values	Drought Category	Probability (%)
$2.00 \leq SPI$	Extremely wet	2.3
$1.50 \leq SPI \leq 1.99$	Severely wet	4.4
$1.00 \leq SPI \leq 1.49$	Moderately wet	9.2
$0.00 \leq SPI \leq 0.99$	Mildly wet	34.1
$-0.99 \leq SPI \leq 0.00$	Mild dry	34.1
$-1.49 \leq SPI \leq -1.00$	Moderate dry	9.2
$-1.99 \leq SPI \leq -1.50$	Severe dry	4.4
$SPI \leq -2.00$	Extreme dry	2.3

## 2.5. The Savitzky-Golay Filter

The Savitzky-Golay (SG) smoothing technique is a prevalent method employed for noise filtration. Savitzky and Golay (1994)

introduced the SG filter as an effective technique for signal smoothing. The SG technique attenuates noise utilising two

250 parameters: polynomial order and window size. By flexibly adjusting these two parameters, the SG filter can achieve

exceptional performance in various pre-processing circumstances. The essence of this procedure involves fitting a low-degree

polynomial to the samples within a sliding window using the least squares method, resulting in a new smoothed value for the

central point derived by convolution. The SG filter is a specific variant of low-pass filter that substitutes each value in the time

series with a new value derived from a polynomial fit to  $2m + 1$  surrounding points, including the point to be smoothed, where

255 m is equal to or larger than the polynomial's order. The polynomial is articulated as follows:

$$p(n) = \sum_{k=0}^N a_k n^k \quad (22)$$

where  $N$  is the power of the polynomial and  $N \leq 2M + 1$ . The following equation is used to determine the error between the estimated and original values; in order to find the desired polynomial result, this error must be minimised.

$$\epsilon_N = \sum_{n=-M}^M (p(n) - x[n])^2 \quad (23)$$

The following form of discrete convolution can be used to express the filter's output:

$$y[n] = \sum_{m=-M}^M h[m] x[n-m] = \sum_{m=n-M}^{n+M} h[n-m] x[m] \quad (24)$$

This work employs the SG filter for two primary reasons: firstly, it enhances system performance by preserving the width and

260 height of waveform peaks in noisy SPI, and secondly, it modifies the SPI while maintaining its fundamental qualities.



## 2.6. The Complete Ensemble Empirical Mode Decomposition with Adaptive Noise.

The model's ability to fit functions and converge will be constrained by the complexity and volatility of the original time sequence, which in turn limits the model's predictive power. To overcome this challenge, the complete ensemble empirical mode decomposition (CEEMDAN) technique is used to pre-process the original nonstationary and nonlinear time sequence.

265 Both empirical mode decomposition (EMD) and ensemble empirical mode decomposition (EEMD), have been enhanced by the CEEMDAN. The computational efficiency is improved, and the reconstructed sequences of both the EMD and EEMD algorithms are free of modal confusion and noise residuals (Zhang et al., 2023). A residual term and a sequence of intrinsic mode functions (IMFs) are the building blocks of a complicated time series signal that the CEEMDAN breaks down.

270 Step 1: Incorporate a constrained quantity of adaptive white noise into the original sequence  $x(t)\delta_0\omega^i(t)$  ( $t = 1, 2, 3, \dots, N$ )  
$$x^i(t) = x(t) + \delta_0\omega^i(t) \quad (25)$$

where  $N$  denotes the number of trials,  $\delta_0$  signifies a coefficient of intensity, and  $\omega^i(t)$  indicates the  $i$ th realisation of a stochastic Gaussian process.

Step 2: The residual  $r_1(t)$  and the first modal component  $IMF_1$  are obtained by decomposing each equation (1) using EMD.

$$\overline{IMF_1(t)} = \frac{1}{N} \sum_{i=1}^N EMD_1(x^i(t)) \quad (26)$$

$$r_1(t) = x(t) - \overline{IMF_1(t)} \quad (27)$$

275

In this context,  $EMD_1(\cdot)$  denotes the initial IMF component produced by the EMD algorithm, while  $r_1(t)$  signifies the residual associated with the first stage.

Step 3: Add white noise  $\delta_1 EMD_1(\omega^i(t))$  to the residual  $r_1(t)$  and further decomposed by EMD to obtain the second modal component  $IMF_2$  and residual  $r_2(t)$ .

$$\overline{IMF_2(t)} = \frac{1}{N} \sum_{i=1}^N EMD_1(r_1(t) + \delta_1 EMD_1(\omega^i(t))) \quad (28)$$

280

$$r_2(t) = r_1(t) - \overline{IMF_2(t)} \quad (29)$$

For the  $j = 3, 4, \dots, N$ , the  $j$ th IMF component and the  $j$ th residual can be computed as:

$$\overline{IMF_j(t)} = \frac{1}{N} \sum_{i=1}^N EMD_1(r_{j-1}(t) + \delta_{j-1} EMD_{j-1}(\omega^i(t))) \quad (30)$$



$$r_j(t) = r_{j-1}(t) - \overline{IMF_j(t)} \quad (31)$$

where  $EMD_{j-1}(\cdot)$  denotes the  $(j - 1)$ th intrinsic mode function component derived from the empirical mode decomposition technique, and  $r_j(t)$  represents the residual following the  $j$ th decomposition.

285 Step 3: Continue executing step 3 until the residual  $r_j(t)$  meets a predetermined termination criterion.

The time series  $x(t)$  can ultimately be articulated as

$$x(t) = \sum_{i=1}^N \overline{IMF_i(t)} + r_N(t) \quad (32)$$

## 2.7. The Autoregressive Integrated Moving Average Model

The Autoregressive Integrated Moving Average (ARIMA) model, pioneered by Box and Jenkins in the 1970s, serves as a 290 robust and effective forecasting approach for time series analysis (Box et al., 2015). The ARIMA model, often known as the Box-Jenkins approach, is depicted through the concepts presented by Sibiya et al. (2024) in Figure 2. The ARIMA models predict future values of the time series as a linear combination of historical and residual data. This model comprises three components: the order of seasonal differentiation, autoregressive order, and moving average order (Montgomery et al., 2015). The backward shift operator  $B$  is employed to eliminate nonstationarity. A time series,  $y_t$ , is called homogeneous nonstationary 295 if its first order difference,  $\omega_y = (1 - B)y_t = y_t - y_{t-1}$  or the  $d$ th difference  $\omega_t = (1 - B)^d y_t$  is also stationary time series. Furthermore,  $y_t$  is referred to as an ARIMA model with orders  $p, d$  and  $q$ , noted  $ARIMA(p, d, q)$ . Hence, an  $ARIMA(p, d, q)$  is often expressed as

$$\phi(B)(1 - B)^d y_t = c + \theta(B)\varepsilon_t \quad (33)$$

$$\phi(B) = 1 - \sum_{i=1}^p \phi_i B^i \quad \text{and} \quad \theta(B) = 1 - \sum_{i=1}^q \theta_i B^i \quad (34)$$

300 The backward shift operators for  $AR(p)$  and  $MA(q)$  are defined as  $\phi(B)y_t = c + \varepsilon_t$  and  $y_t = \mu + \theta(B)\varepsilon_t$  with  $c = \mu - \phi\mu$ , where  $\mu$  and  $\varepsilon_t$  are the mean and white noise, respectively and the  $\varepsilon_t$  is independent and normally distributed with mean 0 and variance of  $\sigma_\varepsilon^2$ .

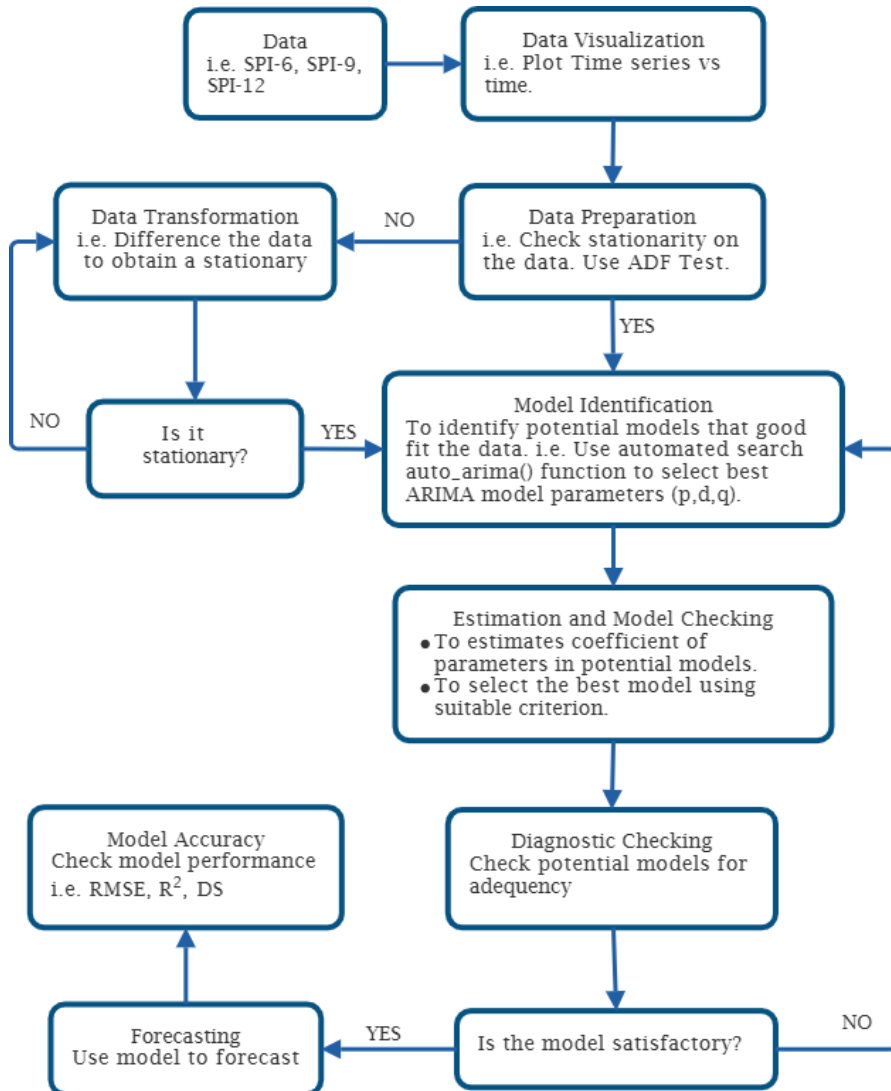


**Figure 2: The Box-Jenkins Steps Approach.**

305

## 2.8. The Long Short-Term Memory

Long short-term memory (LSTM) algorithms represent a category of recurrent neural network (RNN) designs that are proficient in handling sequential input and identifying temporal relationships (Hochreiter and Schmidhuber, 1997). LSTM networks incorporate specific memory cells and gates for the efficient management and regulation of information flow over various time steps. Consequently, they can effectively represent the data input while maintaining essential dependencies and patterns. The LSTM methodology addresses the problem of vanishing gradients encountered by RNN algorithms. This occurs when the gradient diminishes to a level insufficient for effectively updating the weights throughout prolonged sequences. The

310



LSTM facilitates the flow of gradients across time by employing memory cells and gates. The model's foundational design primarily consists of three control gates: input, forget, and output. The activation function is represented by  $\sigma$ , whereas the cell states at time  $t - 1$  and  $t$  are designated as  $C_{t-1}$  and  $C_t$  respectively. At time  $t$  and time  $t - 1$ , the cell possesses two concealed states,  $h_t$  and  $h_{t-1}$ . Figure 3 illustrates the building of the LSTM unit, and the mathematical equations (35) to (40) for the LSTM method are provided below. Initially, by employing the model's forget gate, we may determine the current hidden state  $h_{t-1}$  and the degree to which the input  $x_t$  has been preserved. The formula is

$$f_t = \sigma(W_f x_t + U_f h_{t-1} + b_f) \quad (35)$$

Secondly, the input gate allows us to ascertain the volume of content from the input variable that can be retained in the cell state  $C_t$

$$i_t = \sigma(W_i x_t + U_i h_{t-1} + b_i) \quad (36)$$

$$\tilde{C}_t = \sigma_c(W_c x_t + U_i h_{t-1} + b_i) \quad (37)$$

$$C_t = f_t \odot C_{t-1} + i_t \odot \tilde{C}_t \quad (38)$$

The output gate of the LSTM produces outputs, and the hidden state of each cell is represented by the formula:

$$o_t = \sigma(W_o x_t + U_o h_{t-1} + b_o) \quad (39)$$

$$h_t = o_t \odot \sigma_h(C_t) \quad (40)$$

In the aforementioned formulas,  $W_f$ ,  $W_i$ , and  $W_o$  represent the weight matrices associated with the various control gates. The terms  $b_f$ ,  $b_i$ , and  $b_o$  correspond to the bias terms for each respective control gate. The notation  $\tilde{C}_t$  signifies the complete input activation vector, while the operator  $\odot$  (Hadamard product) indicates the element-wise multiplication of the elements between two vectors. The  $\sigma$  activation function quantifies the amount of information that is transmitted through the various control gates.

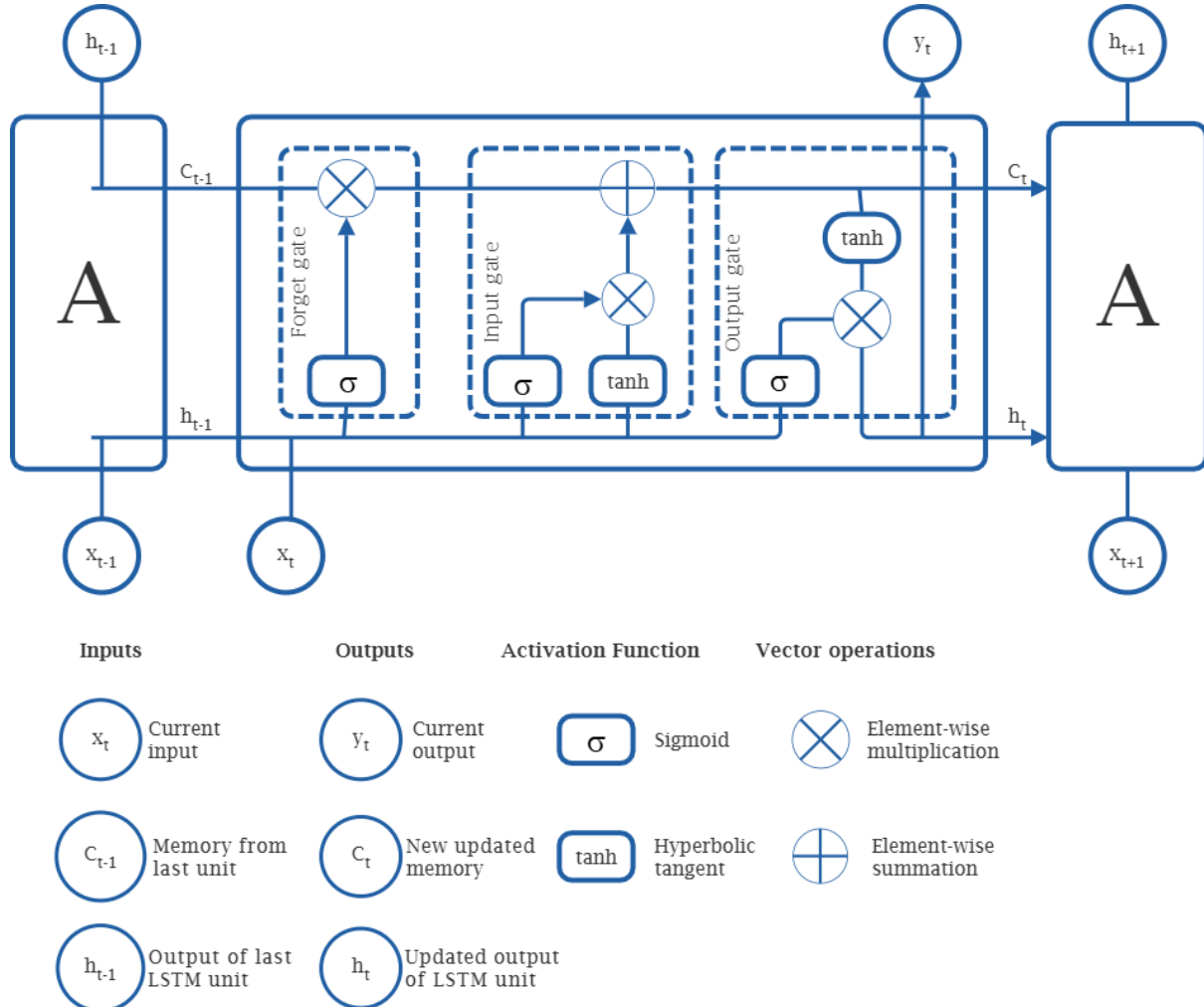


Figure 3: Structure diagram of LSTM model.

### 330 2.9. The ARIMA-LSTM hybrid Model

Achieving accurate estimates of SPI index values through a forecasting model is essential for informed decision-making. Zhang (2003) offers a hybrid model wherein the ARIMA model extracts and predicts linear components, while the residuals, representing nonlinear data subcomponents, are then modelled by the LSTM approach. This study employs a hybrid model that integrates ARIMA and LSTM to predict both linear and nonlinear behaviours with optimal accuracy.

$$\mathcal{H}_t = \mathcal{L}_t + \mathbf{x}_t \quad (41)$$

335 where  $\mathcal{L}_t$  and  $\mathbf{x}_t$  denotes the linear and nonlinear components, respectively, for the hybrid technique which are computed using the initial time series ( $y_t$ ). Consider the original dataset at time t and the forecast results obtained from applying the ARIMA



model as  $\hat{L}_t$  the prediction results. Thus,  $\mathcal{E}_t = y_t - \hat{L}_t$  is the definition of the residual  $\mathcal{E}_t$  that is derived by removing  $\hat{L}_t$  from  $y_t$ . Subsequently we compute the value  $\hat{N}_t$  by feeding the series of residuals into the LSTM model, which predicts the nonlinear component of the values. This equation may be written as

$$\hat{N}_t = f_{LSTM}(\mathcal{E}_{t-1}, \mathcal{E}_{t-2}, \dots, \mathcal{E}_{t-n}) + \epsilon_t, \quad (42)$$

340 where is a nonlinear expression associated with the LSTM model and  $\epsilon_t$  is the random error. The combined forecasts from the two steps were then used to determine the value for the ARIMA-LSTM hybrid model. As illustrated in Figure 4, the equation  $\hat{H}_t = \hat{L}_t + \hat{N}_t$  predicts the linearity and nonlinearity values, respectively, using ARIMA and LSTM models.

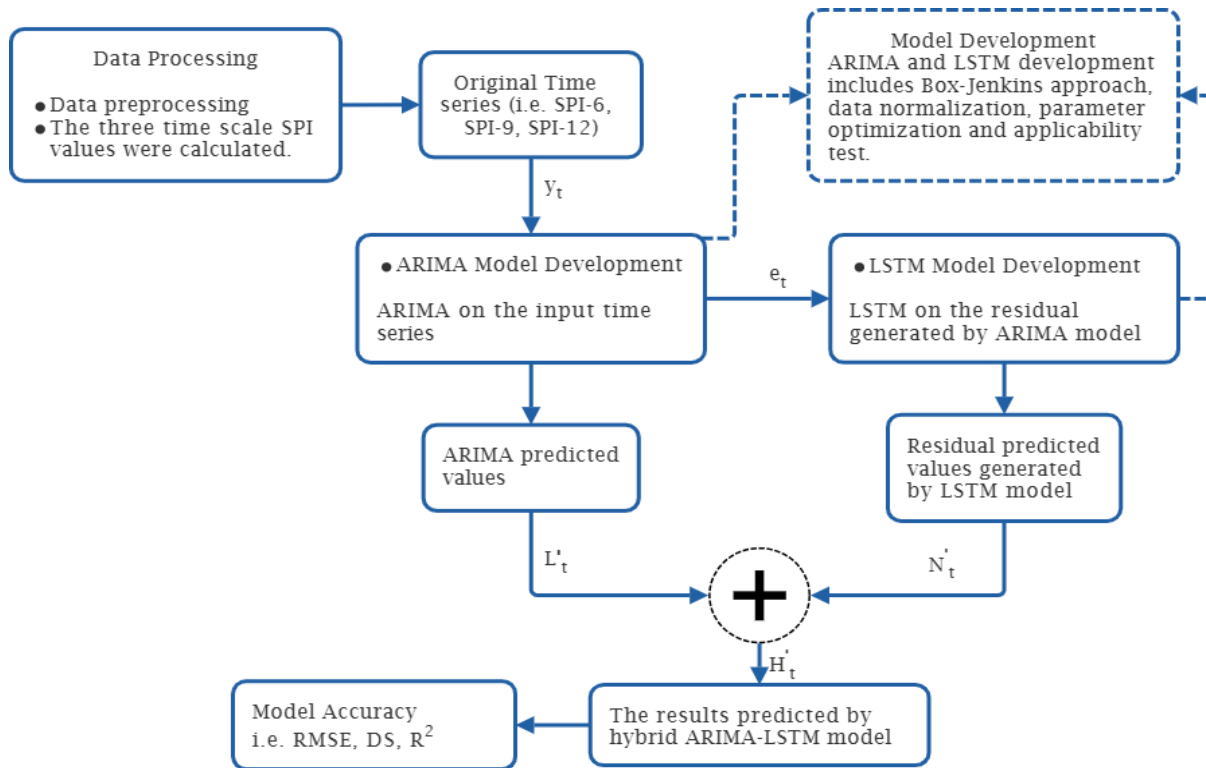


Figure 4: Predictive flowchart of the ARIMA-LSTM hybrid model.

345

## 2.10. The development of the proposed SG-CEEMDAN-ARIMA-LSTM hybrid model

Due to the great uncertainty of the drought data and the existence of complexity, nonlinearity and nonstationary trends, the single prediction model is greatly limited, however the hybrid method has better prediction accuracy. The SG-CEEMDAN-ARIMA-LSTM algorithm that combines different techniques for improved accuracy in predicting drought based on the 350 standardised precipitation index is proposed this study. This hybrid model is designed as a sequential framework where each step refines the data for subsequent modelling. The SG-CEEMDAN pre-processing stage enhances the data by smoothing and



decompose into the meaningful components. The components fed to the ARIMA-LSTM model that involves two-step process: the ARIMA for initial prediction and the LSTM model for refining and enhancing predictions. The hybrid model combines the ARIMA and the LSTM predictions to form the final hybrid forecasts. Figure 5 illustrates the proposed hybrid model 355 algorithm. The process of SPI prediction based on ARIMA-LSTM combined with SG and CEEMDAN as is shown in Figure 5. The process of the data smoothing, decomposition and prediction includes four main steps.

Step 1: Data smoothing and decomposition: SG is first applied to SPI series then CEEMDAN decomposed data to obtain IMFs and residual.

Step 2: A training set and a test are created from sequence that was obtained from step 1.

360 Step 3: Create the SG-CEEMDAN-ARIMA-LSTM prediction model.

Step 4: Evaluate the prediction model. The SG-CEEMDAN-ARIMA-LSTM model is evaluated by statistical criterion and Taylor diagram.

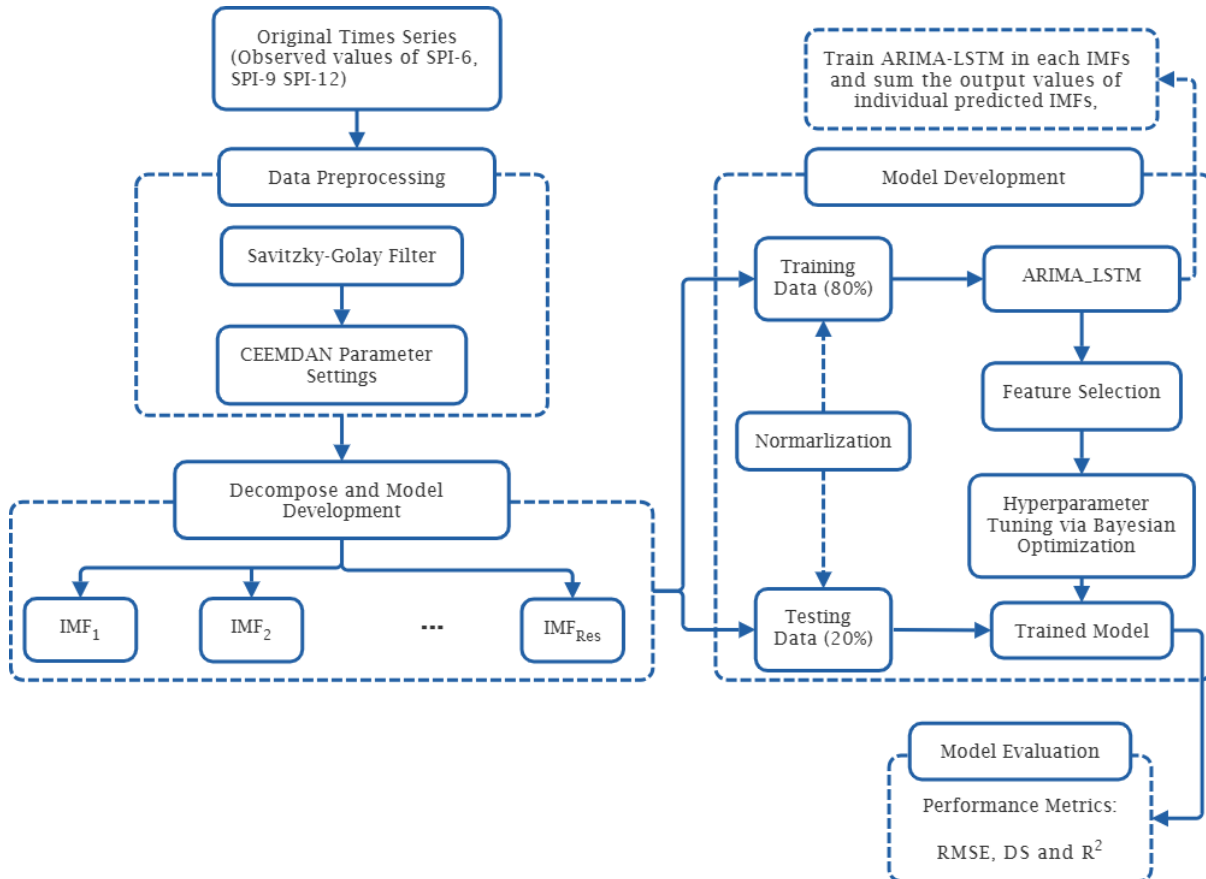


**Figure 5: Procedure of proposed SG-CEEMDAN-ARIMA-LSTM hybrid model.**

365



## 2.11. Performance Evaluation

To establish the predictive superiority of the SG-CEEMDAN-ARIMA-LSTM model, a comparison was conducted against 370 other models, including ARIMA, LSTM, ARIMA-LSTM, SG-ARIMA-LSTM, and CEEMDAN-ARIMA-LSTM models. The performance of the proposed hybrid-based model is evaluated using three indicators namely, root mean square error (RMSE), coefficient of determination ( $R^2$ ) and directional symmetry (DS). The high value of  $R^2$  and DS reflects the better performance of the forecasting model while the lower the value of RMSE illustrates better forecasting performance.

$$RMSE = \sqrt{\frac{1}{n} \sum_{i=1}^n (y_i - \hat{y}_{avg})^2} \quad (43)$$

$$R^2 = \frac{[\sum_{i=1}^n (y_i - y_{avg})(\hat{y}_i - \hat{y}_{avg})]^2}{\sum_{i=1}^n (y_i - y_{avg})^2 \sum_{i=1}^n (\hat{y}_i - \hat{y}_{avg})^2} \quad (44)$$

$$DS = \frac{100}{n-1} \sum_{i=2}^n d_i \quad (45)$$

where

$$d_i = \begin{cases} 1, & (y_i - y_{i-1})(\hat{y}_i - \hat{y}_{i-1}) > 0 \\ 0, & \text{otherwise} \end{cases} \quad (46)$$

375  $n$  is number of data points,  $y_i$  and  $\hat{y}_i$  observed and forecasted, respectively.  $y_{avg}$  and  $\hat{y}_{avg}$  an average of the actual and forecasted values, respectively. Furthermore, this study conducts a qualitative evaluation of the prediction model's performance using a Taylor diagram (Taylor, 2001). The Taylor diagram offers a statistical evaluation of the degree of agreement between the models in terms of their SD, RMSE, and  $R^2$ , while providing a concise summary of the correspondence between predicted and observed values. The differences in SD, RMSE, and  $R^2$  values among the prediction models are depicted as individual 380 points on a two-dimensional plot within the Taylor diagram. This diagram, though it follows a common structure, proves especially valuable when evaluating intricate models.

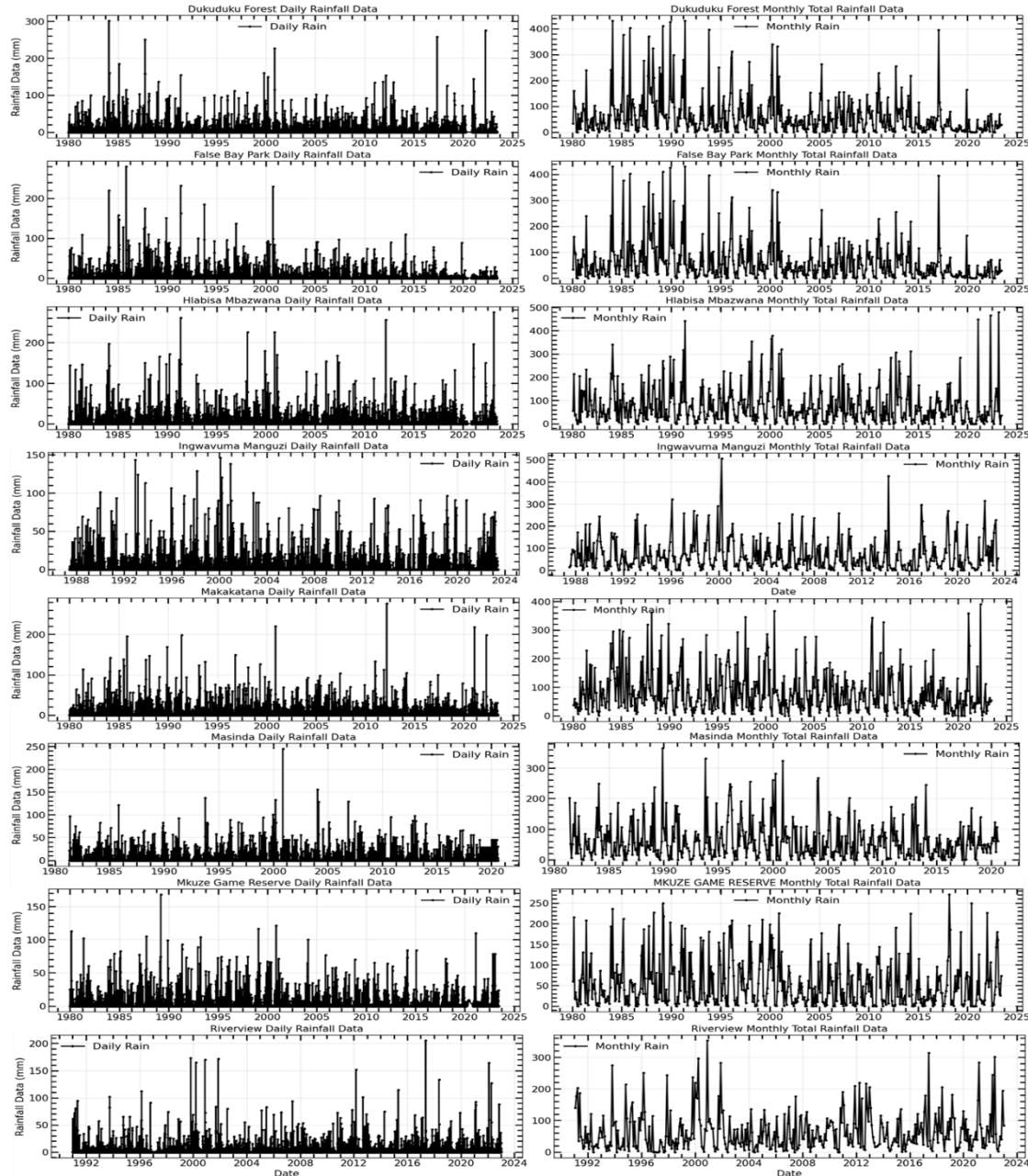
## 3. Results and Discussion

### 3.1. Rainfall Data Series

Figure 6 illustrates the daily and monthly cumulative precipitation data recorded at the uMkhanyakude district meteorological 385 stations in KwaZulu-Natal province, South Africa, from the early 1980s to 2023. The data comprising 20% was employed for prediction, whereas the data representing 80% was applied for training. The SPI computed utilising rainfall data from



meteorological stations in the uMkhanyakude district, which provide sufficiently extensive records and a consistent structure (Hirca et al., 2022).





395 3.2. SPI Time Series and Trend Analysis

This study SPI values for the 6-, 9-, and 12-month intervals were computed using the monthly mean time series shown in Figure 6. Figure 7 illustrates the time series of the SPI calculated for the 6-month (SPI-6), 9-month (SPI-9), and 12-month (SPI-12) intervals. All SPIs (SPI-6, SPI-9, and SPI-12) demonstrate numerous occurrences of moderate to severe droughts in the studied area. A significant drought episode was reported from late 2004 to 2009. Moreover, SPI-12 demonstrates a 400 persistent drought spell that began between 2014 and 2016, leading to a decline in water supply conditions in the region (Bukhosini and Moyo, 2023). The statistics across all timelines indicate a troubling trend of extended and intense drought conditions in recent years. This underscores the pressing necessity for efficient water management and drought readiness in the area. Initially, we assess the trend throughout the research area employing nonparametric techniques. The ensuing conclusions will be obtained via advanced trend analysis methods employed to investigate SPI trends.

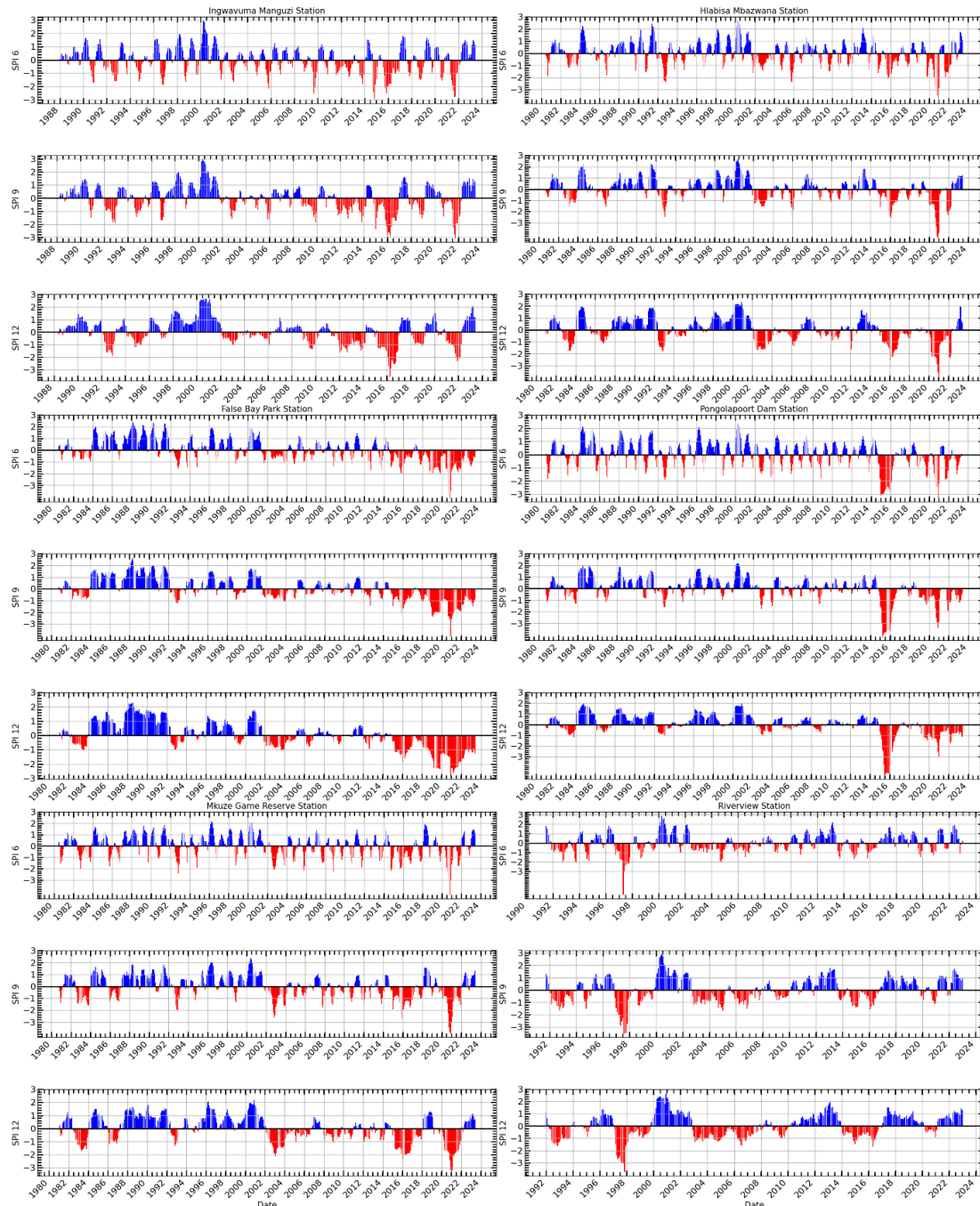


**Figure 7: Standardized Precipitation Index (SPI) time series plots for uMkhanyakude district over 6-month (SPI-6), 9-month (SPI-9), and 12-month (SPI-12) periods from early 1980's to 2023. Positive SPI values (blue bars) indicate wetter-than-normal conditions, while negative SPI values (red bars) indicate drier-than-normal conditions.**



410 Figure 8 illustrates the regional outcomes of the ITA methodology used to the 6-, 9-, and 12-month SPI series to ascertain the potential meteorological drought trend in the uMkhanyakude district. Figure 8 includes two vertical bands to elucidate the potential trends of arid and humid conditions: a red band indicating the drought threshold ( $SPI = -1.5$ ) and a blue band denoting the wet threshold ( $SPI = 1.5$ ). The zone between the two bands signifies normal conditions, hence facilitating the depiction of both low and high SPI trends using the ITA methodology. Each plot compares the first and second halves of the data series to  
415 identify trends.

In general, for both Figure 8 and Table 3 all stations except Riverview indicate downwards trend for all time scales, in terms of the ITA. For an example, the ITA results obtained using 6-month SPI values exhibit a slightly decreasing trend in precipitation, moving toward the upper right quadrant, indicating the detection of dryer conditions over the 6-month timescale.

420 Some points approach the severely wet threshold but do not cross it, indicating that there were no extreme wet periods, though some drier periods are evident near the severe dry line. The ITA results obtained using 9-month SPI values shows a more pronounced decreasing trend, indicates a relatively weaker increase in wet conditions over a 9-month timescale. Several points come close to the severe dry threshold, but the data remains mostly within the 95% confidence bounds, indicating moderate variability in precipitation trends. On the other hand, the SPI-12 plot demonstrates a noticeable decreasing trend toward  
425 dryness, as many points fall below the no-trend line and approach the severe dry region. Riverview indicates the increasing trend across all time scales. The increasing distance between the black dots and the no-trend line highlights a shift toward drier conditions in the second half of the series. In general, the analysis suggests a gradual increase in precipitation for shorter periods (SPI-6), moderate upward trends for medium-term periods (SPI-9), and a more substantial shift toward dry conditions over longer periods (SPI-12) for Riverview. The variability is evident, but there is a clear progression toward drier conditions,  
430 particularly in the SPI-12 plot. This observation could be indicative of changing precipitation patterns, which is crucial for understanding drought risk and informing water resource management strategies.

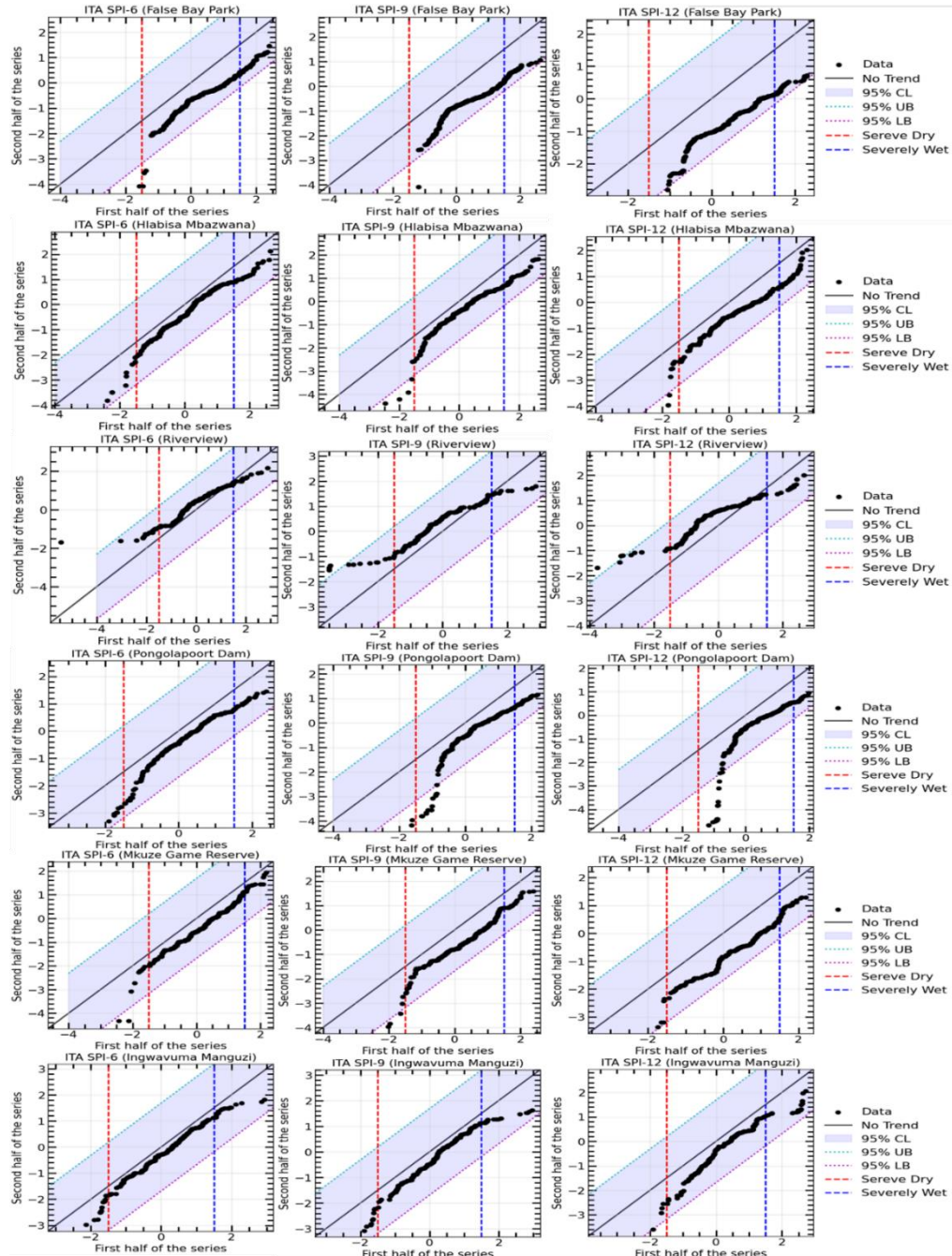


**Figure 8: Results of Innovative trend analysis applied to different time scales values (SPI-6 (left), SPI-9 (middle), SPI-12 (right)).**

The blue shaded area represents the 95% confidence level area. The red and blue vertical lines represent the severe drought and severely wet, respectively.



Table 2 presents the results of the Mann-Kendall (MK) and Modified Mann-Kendall (MMK) trend tests for the Standardized Precipitation Index (SPI) over 6-month (SPI-6), 9-month (SPI-9), and 12-month (SPI-12) periods. The results indicate that across five stations all time scales both MK and MMK methods showed significant decreasing trend with negative Z-score values. For example, False Bay Park,  $Z_{MK}$  are  $Z_{SPI-6} = -10.89$ ,  $Z_{SPI-9} = -12.89$ ,  $Z_{SPI-12} = -13.82$  and  $Z_{MMK}$  are  $Z_{SPI-6} = -6.27$ ,  $Z_{SPI-9} = -6.28$ ,  $Z_{SPI-12} = -6.29$ . The p-values of MK and MMK show the significance of the trends, with values way below 0.05 confirming statistically significant trends. In all cases except Riverview, the p-values are extremely low ( $<< 0.05$ ), indicating strong evidence of significant decreasing trends in precipitation for all SPI periods. Both the MK and MMK tests confirm decreasing trends across all time scales, with the  $Z_{MK}$  and  $Z_{MMK}$  values becoming more negative as the SPI period increases, reflecting an intensifying downward trend over longer periods (from SPI-6 to SPI-12). For Riverview station, the results indicate an increasing trend with positive Z-score values, i.e.  $Z_{MK}$  are  $Z_{SPI-6} = 2.85$ ,  $Z_{SPI-9} = 3.84$ ,  $Z_{SPI-12} = 4.59$  and  $Z_{MMK}$  are  $Z_{SPI-6} = 1.19$ ,  $Z_{SPI-9} = 2.16$ ,  $Z_{SPI-12} = 2.29$ . In general, all these results are consistent with those shown using the ITA (see Table 3). The Riverview station experience increasing trend because it is located closer to the coast, hence it is influenced by a combination of geographic, oceanic and climatic factors. For an example, this station could be influenced by the Agulhas Current, which flows southwards along the east coast of South Africa, bringing warm, moist air from the Indian Ocean, and thus enhancing evaporation that brings constant availability of moisture in the atmosphere.

**Table 2: Statistical summary of trend analysis for SPI-6, SPI-9, and SPI-12 using Mann-Kendall (MK) and Modified Mann-Kendall (MMK) tests.**

False Bay Park			
Variables	SPI-6	SPI-9	SPI-12
$Z_{MK}$	-10.89	-12.89	-13.82
$p - value_{MK}$	$< 0.00$	$< 0.00$	$< 0.00$
Decision ( $Trend_{MK}$ )	Decreasing	Decreasing	Decreasing
$Z_{MMK}$	-6.27	-6.28	-6.29
$p - value_{MMK}$	$3.66 \times 10^{-10}$	$3.35 \times 10^{-10}$	$3.13 \times 10^{-10}$
Decision ( $Trend_{MMK}$ )	Decreasing	Decreasing	Decreasing
Hlabisa Mbazwana			
$Z_{MK}$	-2.89	-3.88	-5.31
$p - value_{MK}$	$3.77 \times 10^{-3}$	$3.05 \times 10^{-4}$	$1.10 \times 10^{-7}$
Decision ( $Trend_{MK}$ )	Decreasing	Decreasing	Decreasing
$Z_{MMK}$	-2.26	-2.12	-2.20
$p - value_{MMK}$	$2.39 \times 10^{-2}$	$3.36 \times 10^{-2}$	$2.78 \times 10^{-2}$



Decision ( $Trend_{MK}$ )	Decreasing	Decreasing	Decreasing
<b>Pongolapoort Dam</b>			
$Z_{MK}$	-7.19	-8.74	-9.83
$p - value_{MK}$	$6.12 \times 10^{-13}$	< 0.00	< 0.00
Decision ( $Trend_{MK}$ )	Decreasing	Decreasing	Decreasing
$Z_{MMK}$	-8.22	-5.44	-6.51
$p - value_{MMK}$	$2.22 \times 10^{-16}$	$5.40 \times 10^{-8}$	$7.41 \times 10^{-11}$
Decision ( $Trend_{MK}$ )	Decreasing	Decreasing	Decreasing
<b>Mkuze Game Reserve</b>			
$Z_{MK}$	-3.66	-5.54	-6.67
$p - value_{MK}$	$2.48 \times 10^{-4}$	$2.99 \times 10^{-8}$	$2.55 \times 10^{-11}$
Decision ( $Trend_{MK}$ )	Decreasing	Decreasing	Decreasing
$Z_{MMK}$	-2.44	-2.79	-2.22
$p - value_{MMK}$	$1.46 \times 10^{-2}$	$5.13 \times 10^{-3}$	$2.64 \times 10^{-2}$
Decision ( $Trend_{MK}$ )	Decreasing	Decreasing	Decreasing
<b>Ingwavuma Manguzi</b>			
$Z_{MK}$	-2.38	-3.72	-4.92
$p - value_{MK}$	$1.72 \times 10^{-2}$	$1.98 \times 10^{-4}$	$8.72 \times 10^{-7}$
Decision ( $Trend_{MK}$ )	Decreasing	Decreasing	Decreasing
$Z_{MMK}$	-1.61	-2.48	-2.27
$p - value_{MMK}$	$1.08 \times 10^{-1}$	$1.31 \times 10^{-2}$	$2.29 \times 10^{-2}$
Decision ( $Trend_{MK}$ )	Decreasing	Decreasing	Decreasing
<b>Riverview</b>			
$Z_{MK}$	2.85	3.84	4.59
$p - value_{MK}$	$4.34 \times 10^{-3}$	$1.25 \times 10^{-4}$	$4.25 \times 10^{-6}$
Decision ( $Trend_{MK}$ )	Increasing	Increasing	Increasing
$Z_{MMK}$	1.94	2.16	2.29
$p - value_{MMK}$	$5.12 \times 10^{-2}$	$3.07 \times 10^{-2}$	$2.19 \times 10^{-2}$
Decision ( $Trend_{MK}$ )	Increasing	Increasing	Increasing

**Table 3: The results of the trend analysis for SPI-6, SPI-9, and SPI-12 obtained through a two-tailed test at a significance level of 5% using ITA technique.**

False Bay Park



Variables	SPI-6	SPI-9	SPI-12
Slope	$-3.51 \times 10^{-3}$	$-1.14 \times 10^{-3}$	$-4.49 \times 10^{-3}$
Indicator	-20.08	-20.12	-20.07
$\pm$ CI at 95%	$\pm 9.24 \times 10^{-5}$	$\pm 7.52 \times 10^{-5}$	$\pm 6.82 \times 10^{-5}$
<b>Hlabisa Mbazwana</b>			
Slope	$-1.68 \times 10^{-3}$	$-2.31 \times 10^{-3}$	$-1.86 \times 10^{-3}$
Indicator	-20.52	-20.72	-20.64
$\pm$ CI at 95%	$\pm 6.81 \times 10^{-5}$	$\pm 9.35 \times 10^{-5}$	$\pm 7.15 \times 10^{-5}$
<b>Pongolapoort Dam</b>			
Slope	$2.26 \times 10^{-3}$	$-2.88 \times 10^{-3}$	$-3.34 \times 10^{-3}$
Indicator	-19.27	-19.40	-19.55
$\pm$ CI at 95%	$\pm 2.22 \times 10^{-5}$	$\pm 3.62 \times 10^{-5}$	$\pm 6.72 \times 10^{-5}$
<b>Mkuze Game Reserve</b>			
Slope	$-2.00 \times 10^{-3}$	$-3.04 \times 10^{-3}$	$-3.80 \times 10^{-3}$
Indicator	-20.09	-20.22	-20.25
$\pm$ CI at 95%	$\pm 2.81 \times 10^{-3}$	$\pm 4.67 \times 10^{-3}$	$\pm 4.40 \times 10^{-3}$
<b>Ingwavuma Manguzi</b>			
Slope	$-1.61 \times 10^{-3}$	$-2.26 \times 10^{-3}$	$-2.88 \times 10^{-3}$
Indicator	-21.96	-21.05	-20.77
$\pm$ CI at 95%	$\pm 6.81 \times 10^{-5}$	$1.01 \pm \times 10^{-5}$	$\pm 1.19 \times 10^{-5}$
<b>Riverview</b>			
Slope	$1.69 \times 10^{-3}$	$2.19 \times 10^{-3}$	$2.37 \times 10^{-3}$
Indicator	22.54	22.22	21.86
$\pm$ CI at 95%	$\pm 1.54 \times 10^{-5}$	$\pm 1.35 \times 10^{-5}$	$\pm 1.56 \times 10^{-5}$

### 460 3.3. SPI Time Series Forecasting Results

The study proposes a hybrid model that applies the Savitzky-Golay (SG) filter to raw SPI data to reduce noise and improve forecasting analysis. To demonstrate the effectiveness of the SG filter, appropriate parameters such as window size and polynomial order were selected through trial and error using data from the study sites (Sibiya et al., 2024). A window size of 465 21 and a polynomial order of 5 were chosen for smoothing. Figure 9 shows how the SG filter effectively tracks the general trend while preserving the shape of peaks and minimizing noise. This filter was applied to different time scales of the SPI time series. It autonomously calibrates according to peak distribution, exhibiting optimal performance, particularly with asymmetric peaks, while preserving peak height integrity. The application of the SG filter effectively mitigates short-term fluctuations and eliminates noise from the time series resulting in cleaner data, thereby enhancing the reliability of the subsequent decomposition process. By reducing noise, decomposition techniques can more accurately capture the authentic underlying 470 patterns and components within the data.

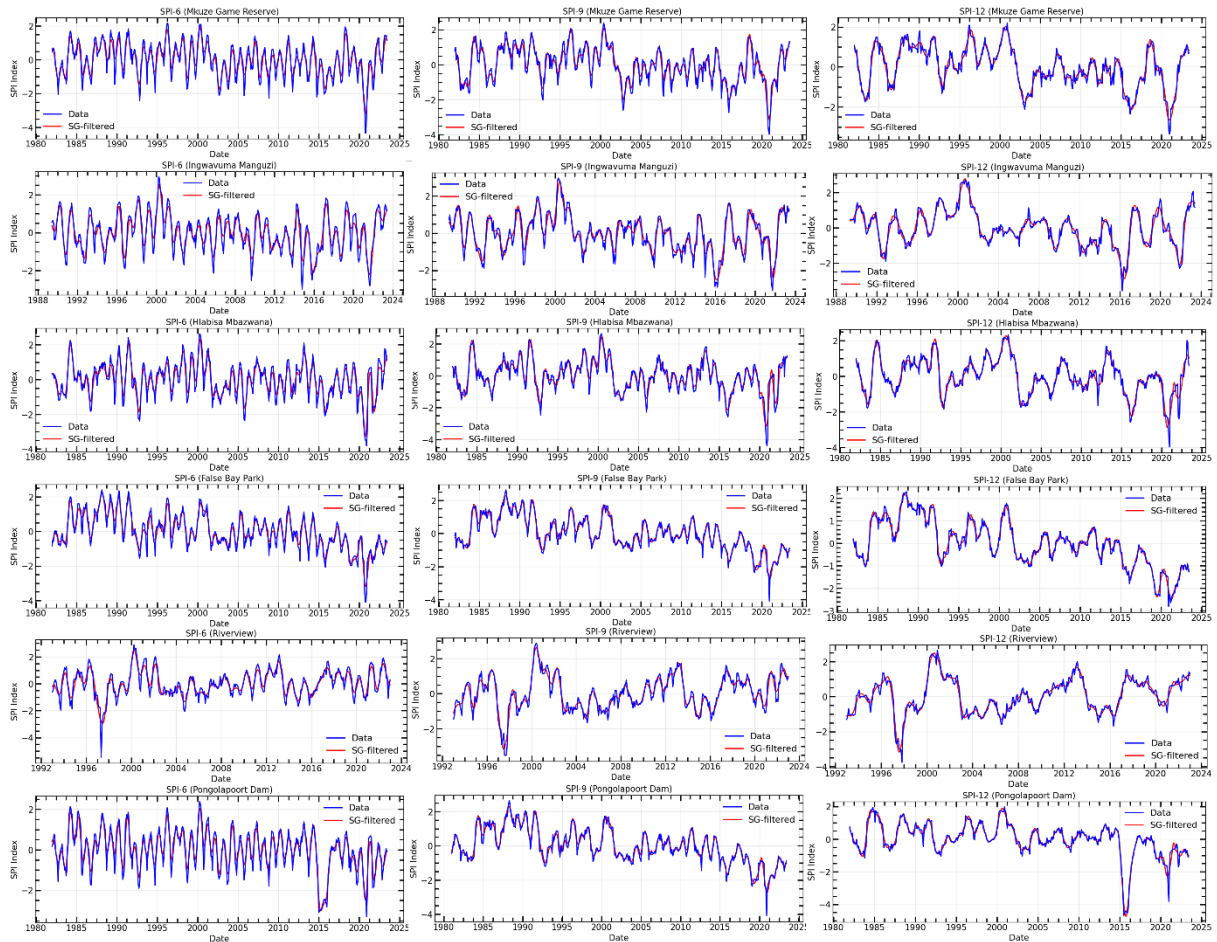
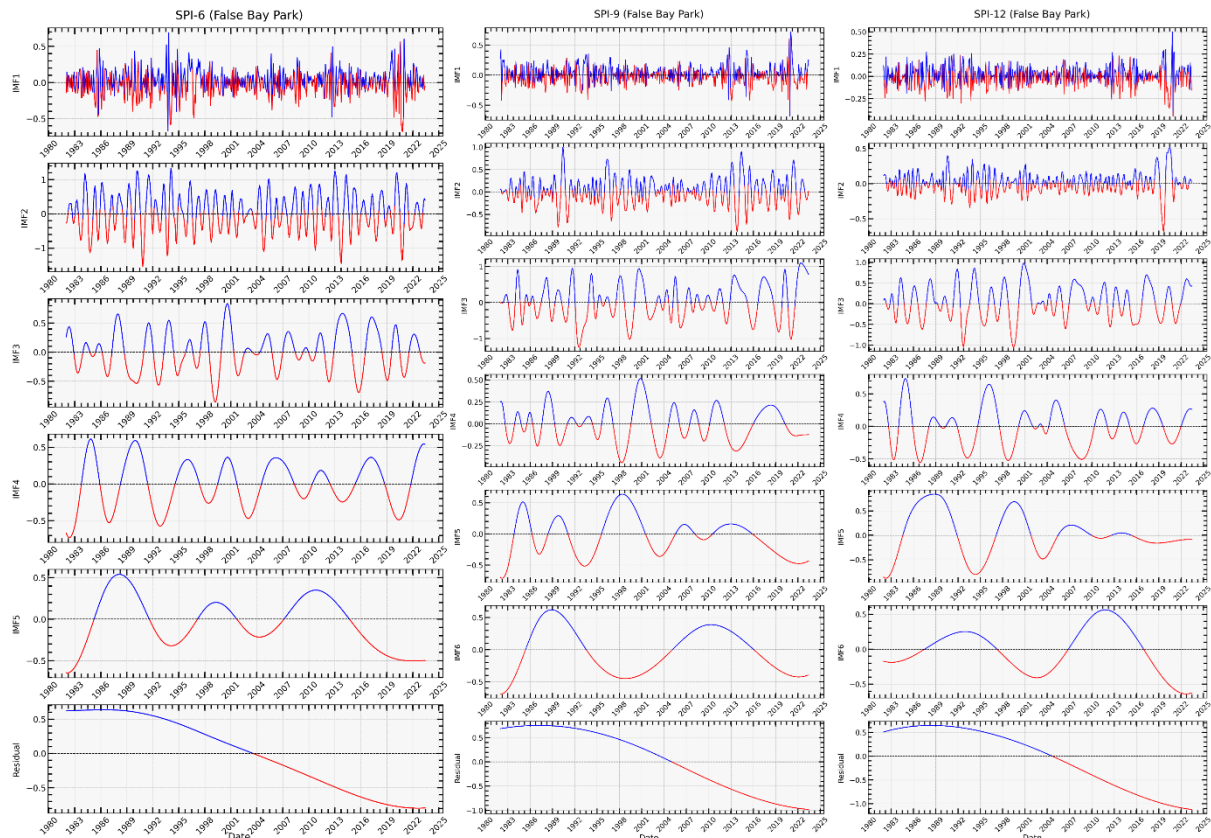


**Figure 9: SPI signals smoothed by Savitzky-Golay (SG). The blue line represents the original signal and red line is the SG smoothed signal.**

475 After applying a Savitzky-Golay filter to the series, the CEEMDAN algorithm decomposes the filtered SPI series into six subseries with different amplitudes and frequencies. The results from the False Bay Park station are utilized here as an illustration to prevent repetition. In these results, the decomposed set of time series consists of five IMF components and a residual component, as shown in Figure 10 (for all time scales). During the decomposition process, white Gaussian noise is added to create noisy signals. The original sequence exhibits high nonlinearity and nonstationarity, with the frequency of the 480 IMF components gradually decreasing. Figure 10 depicts this gradual decrease in frequency as the order of the IMF components increases. As each IMF is further decomposed, it becomes less volatile and cyclical, which aligns with the characteristics of the decomposed IMF. Therefore, by predicting each IMF and the residual, the forecast precision can be enhanced. A forecasting model is then constructed for each component, and the prediction results are obtained by summing up the outputs of all predicted components.



485

**Figure 10: Decomposition of Smoothed SPI-6, SPI-9 and SPI-12 Index Using CEEMDAN: Each IMF represents different frequency components of the SPI index, from high-frequency oscillations (IMF1) to low-frequency trends (IMF5), showing the variability in precipitation patterns over the years from 1980 to 2023.**

490 The models in Table 4 were compared for their prediction ability before and after time series decomposition in this research. The objective was to determine if smoothing and decomposing time series improves the model's prediction performance. Figures 11–16 show a comparison of the various models' prediction outcomes using the Taylor diagram. In general, all the models accurately replicate the original SPI time series at all timescales (refer to Figure 11 - 16) in terms of the time series plot. However, the SG-CEEMDAN-ARIMA-LSTM model (shown in red) appears to have the closest fit to the data, displaying 495 superior accuracy across different phases, particularly in extreme values. Nonetheless, the hybrid models (SG-ARIMA-LSTM, CEEMDAN-ARIMA-LSTM, and SG-CEEMDAN-ARIMA-LSTM) show better precision in capturing peaks, rapid transitions and troughs compared to the standalone LSTM or ARIMA models. Table 4 displays an assessment of the predictive performance metrics of several models utilising RMSE,  $R^2$ , and DS. As the period extends, the RMSE values decrease, however the DS and  $R^2$  values typically enhance (see Table 4). This indicates that the models' predictive accuracy 500 progressively enhances with an extended duration, reaching its highest point at the 12-month interval. In terms of RMSE, the SG-CEEMDAN-ARIMA-LSTM model outperforms the others, exhibiting the lowest error values across all indices. For



example, Riverview station, 0.2165 for SPI-6, 0.0921 for SPI-9, and 0.0566 for SPI-12. This indicates that this model has the smallest prediction error, making it the most accurate in terms of error reduction. Concerning  $R^2$ , which measures how well the model explains the variance in the data, SG-CEEMDAN-ARIMA-LSTM again leads with the highest values: 0.9602 for 505 SPI-6, 0.9846 for SPI-9, and 0.9939 for SPI-12. This shows that the model provides the best fit to the data. The CEEMDAN-ARIMA-LSTM model is the second-best performer, also exhibiting impressive results, particularly in  $R^2$ , where it achieves higher values of 0.9483 for SPI-6, 0.9751 for SPI-9, and 0.9933 for SPI-12. The SG-ARIMA-LSTM model is the third-best hybrid performer, with RMSE values of 0.2262 for SPI-6, 0.1051 for SPI-9, and 0.05639 for SPI-12. The SG-ARIMA-LSTM model is the third-best performer, also exhibiting impressive results, particularly in  $R^2$ , where it achieves higher values of 510 0.9392 for SPI-6, 0.9763 for SPI-9, and 0.9904 for SPI-12. The SG-ARIMA-LSTM model is the third-best hybrid performer, with RMSE values of 0.2597 for SPI-6, 0.1157 for SPI-9, and 0.0567 for SPI-12. In general, these results highlight the efficacy 515 of hybrid models, particularly those incorporating SG and CEEMDAN processes, in improving predictive accuracy across multiple timescales of SPI, particularly for the SG-CEEMDAN-ARIMA-LSTM model. These results are consistent with Taylor diagram (see Figure 11 - 16) which indicates a significant improvement in prediction accuracy after incorporating the 520 SG and CEEMDAN signal decomposition technique as the hybrid model exhibits superior performance in terms of prediction accuracy across all timescales, surpassing other models. This suggests that the inclusion of these techniques enhances the models' ability to capture both short-term and long-term dependencies, thus making them more robust for drought prediction purposes. Therefore, this hybrid model appears to be the most effective for drought prediction in this analysis. These findings highlight the superiority of the proposed hybrid model in enhancing drought prediction accuracy compared to standalone approaches.

**Table 4. Performance measures for the comparison of observed and forecasted data of the models for SPI-6, SPI-9 and SPI-12 across various lead times using statistical criteria.**

Model	False Bay Park								
	SPI-6			SPI-9			SPI-12		
	RMSE	$R^2$	DS	RMSE	$R^2$	DS	RMSE	$R^2$	DS
ARIMA	0.3504	0.8435	0.8426	0.2431	0.8976	0.8525	0.1689	0.9421	0.8426
LSTM	0.3128	0.9111	0.8327	0.2416	0.9521	0.8723	0.1626	0.9821	0.8519
ARIMA-LSTM	0.2476	0.9194	0.8327	0.1650	0.9531	0.8723	0.0507	0.9952	0.9009
SG- ARIMA- LSTM	0.2056	0.9458	0.8030	0.1348	0.9687	0.8218	0.0571	0.9940	0.9009
C-A-L	0.2182	0.9375	0.8713	0.0978	0.9834	0.8218	0.0496	0.9953	0.8911
SG-C-A-L	0.1835	0.9650	0.8416	0.1631	0.9836	0.8317	0.0349	0.9957	0.8941

Mkuze Game Reserve



ARIMA	0.3752	0.8642	0.8419	0.3475	0.8957	0.8792	0.2202	0.9697	0.8730
LSTM	0.3474	0.9121	0.8822	0.3354	0.9178	0.8030	0.1523	0.9890	0.8733
ARIMA-LSTM	0.3160	0.9273	0.8416	0.1561	0.9823	0.8218	0.1079	0.9926	0.8730
SG- ARIMA-LSTM	0.2307	0.9624	0.8515	0.1548	0.9825	0.8317	0.08252	0.9951	0.8019
C-A-L	0.1969	0.9726	0.8317	0.1430	0.9850	0.8515	0.04497	0.9986	0.9208
SG-C-A-L	0.1818	0.9742	0.8515	0.1232	0.9892	0.8617	0.04217	0.9990	0.9208
Pongolapoort Dam									
ARIMA	0.4470	0.8797	0.8624	0.2993	0.9668	0.8119	0.1918	0.9763	0.8733
LSTM	0.4470	0.8962	0.8732	0.2873	0.9467	0.8238	0.1824	0.9851	0.8829
ARIMA-LSTM	0.4121	0.8969	0.8822	0.2599	0.9588	0.8921	0.1638	0.9862	0.8432
SG- ARIMA-LSTM	0.2224	0.9617	0.8019	0.2064	0.9803	0.8515	0.0686	0.9969	0.8119
C-A-L	0.2132	0.9649	0.8822	0.1572	0.9850	0.8218	0.0639	0.9975	0.8019
SG-C-A-L	0.1453	0.9839	0.8824	0.1429	0.9858	0.8911	0.0635	0.9978	0.8921
Hlabisa Mbazwana									
ARIMA	0.4704	0.8347	0.8624	0.4234	0.8698	0.8921	0.2321	0.9556	0.8142
LSTM	0.3617	0.9041	0.8327	0.2163	0.9672	0.8119	0.1566	0.9806	0.8317
ARIMA-LSTM	0.3269	0.9369	0.8515	0.2139	0.9677	0.8218	0.1457	0.9813	0.8426
SG- ARIMA-LSTM	0.3011	0.9355	0.8416	0.1829	0.9747	0.8317	0.08540	0.9935	0.8218
C-A-L	0.2497	0.9592	0.8218	0.1662	0.9792	0.8218	0.0825	0.9949	0.9009
SG-C-A-L	0.1921	0.9795	0.8614	0.1332	0.9866	0.8218	0.07416	0.9952	0.9029
Ingwavuma Manguzi									
ARIMA	0.4123	0.8716	0.8571	0.2706	0.9442	0.8750	0.2052	0.9784	0.8619
LSTM	0.3843	0.8931	0.8738	0.2524	0.2524	0.8691	0.1614	0.9828	0.8095
ARIMA-LSTM	0.3458	0.9044	0.8095	0.2428	0.9695	0.8541	0.8541	0.9847	0.8215
SG- ARIMA-LSTM	0.2767	0.9397	0.8076	0.2001	0.9724	0.8809	0.0815	0.9958	0.8929
C-A-L	0.2536	0.9503	0.8095	0.1945	0.9719	0.8214	0.0739	0.9972	0.9167
SG-C-A-L	0.2314	0.9565	0.8214	0.1575	0.9823	0.8809	0.0634	0.9978	0.8809
Riverview									
ARIMA	0.4375	0.8132	0.8106	0.1708	0.9474	0.8038	0.1137	0.9570	0.7973



LSTM	0.3212	0.8510	0.8108	0.1537	0.9400	0.8108	0.0982	0.9705	0.8273
ARIMA-LSTM	0.2874	0.8767	0.8378	0.1314	0.9706	0.9595	0.0558	0.9934	0.9189
SG- ARIMA-LSTM	0.2262	0.9392	0.8243	0.1051	0.9763	0.8243	0.05639	0.9904	0.8108
C-A-L	0.2597	0.9483	0.8738	0.1157	0.9751	0.9324	0.05674	0.9933	0.9459
SG-C-A-L	0.2165	0.9602	0.8919	0.09214	0.9846	0.9324	0.05664	0.9939	0.9189

Note: C-A-L = CEEMDAN-ARIMA-LSTM

525

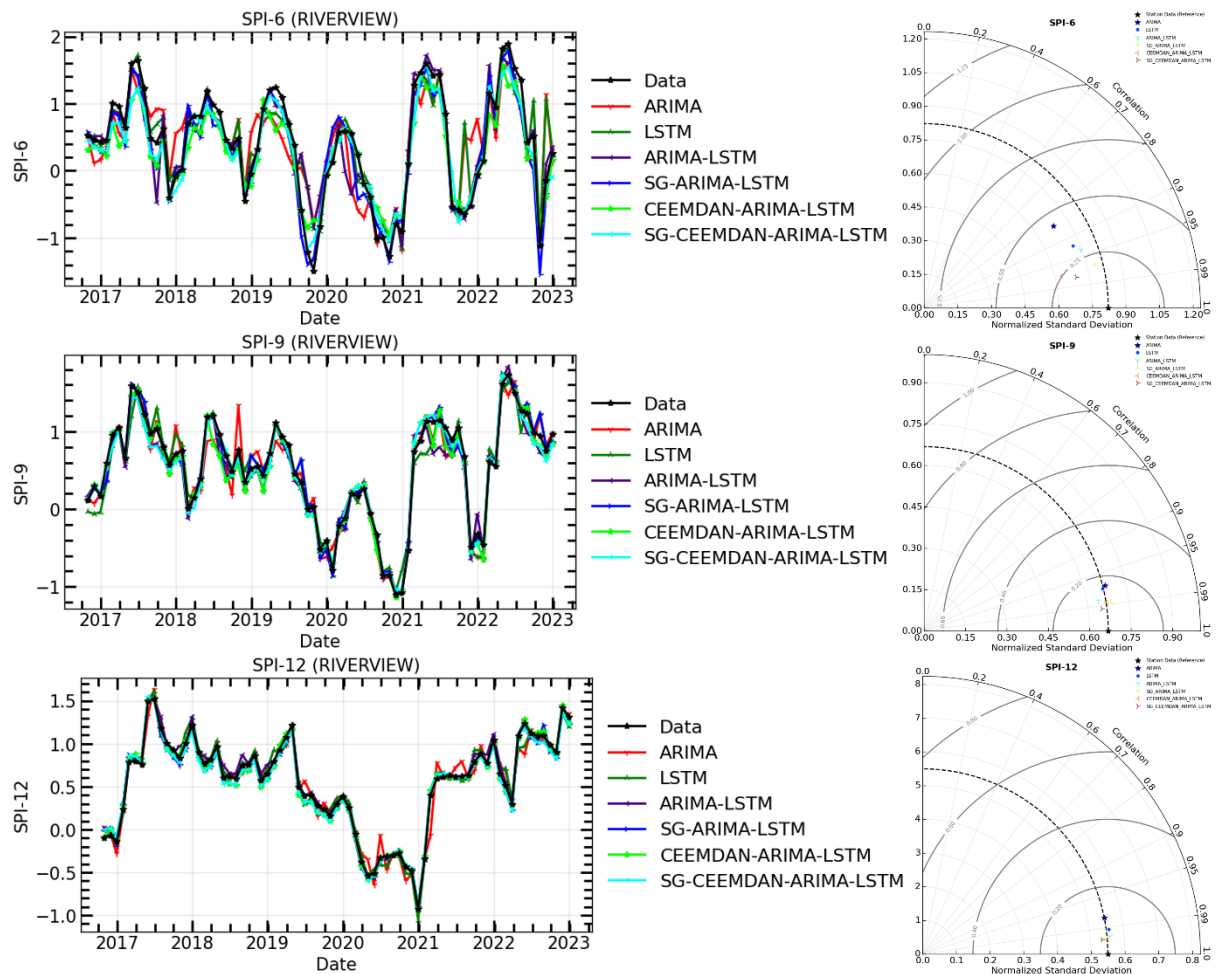
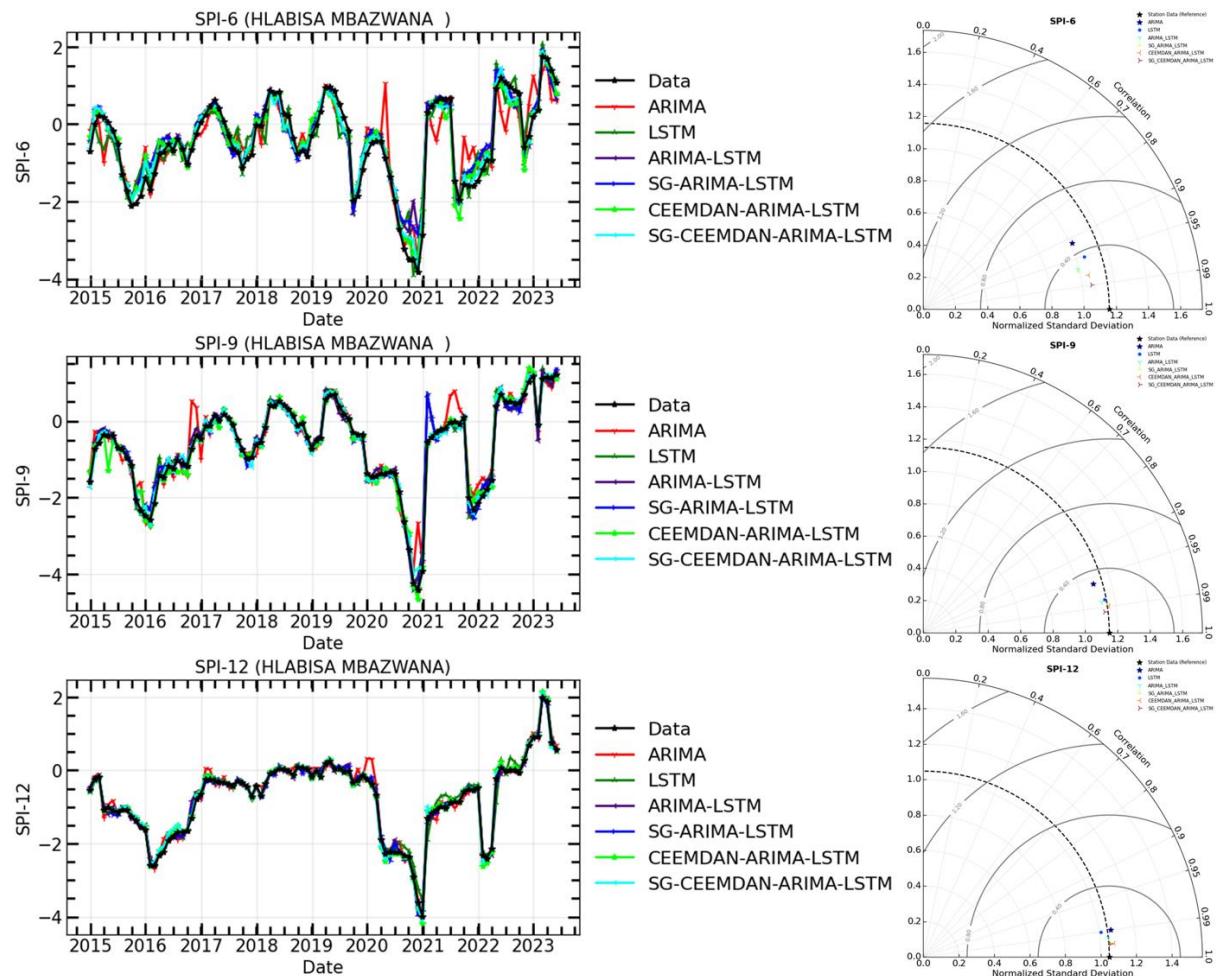


**Figure 11: The time series of observations and hybrid forecasting models for SPI prediction (Left) and their Taylor diagram plots at different timescales (Right) for SPI-6, SPI-9, and SPI-12 of Riverview meteorological station.**



530

**Figure 12: The time series of observations and hybrid forecasting models for SPI prediction (Left) and their Taylor diagram plots at different timescales (Right) for SPI-6, SPI-9, and SPI-12 of Hlabisa Mbazwana meteorological station.**

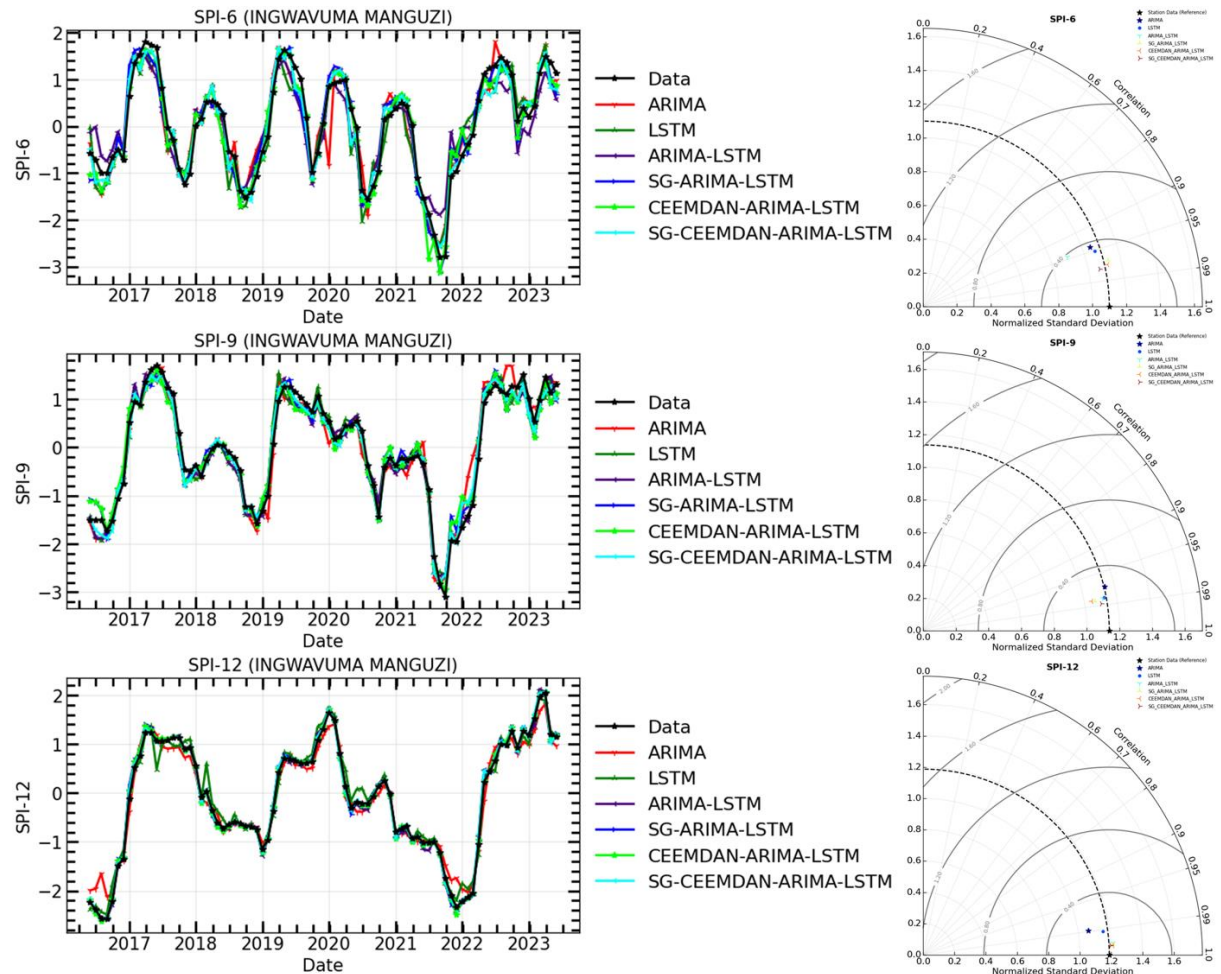


Figure 13: The time series of observations and hybrid forecasting models for SPI prediction (Left) and their Taylor diagram plots at different timescales (Right) for SPI-6, SPI-9, and SPI-12 of Ingwavuma Mangazi meteorological station.

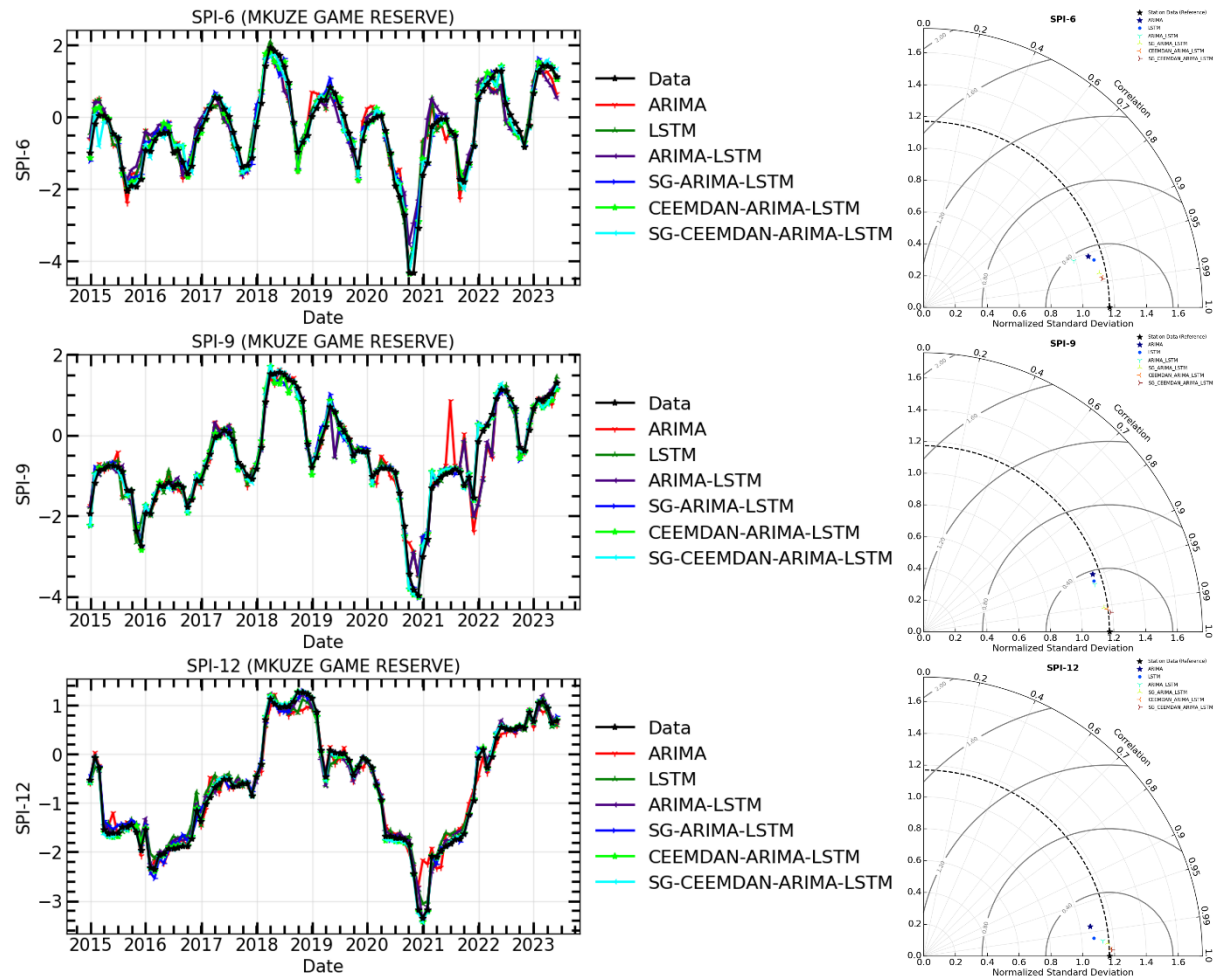
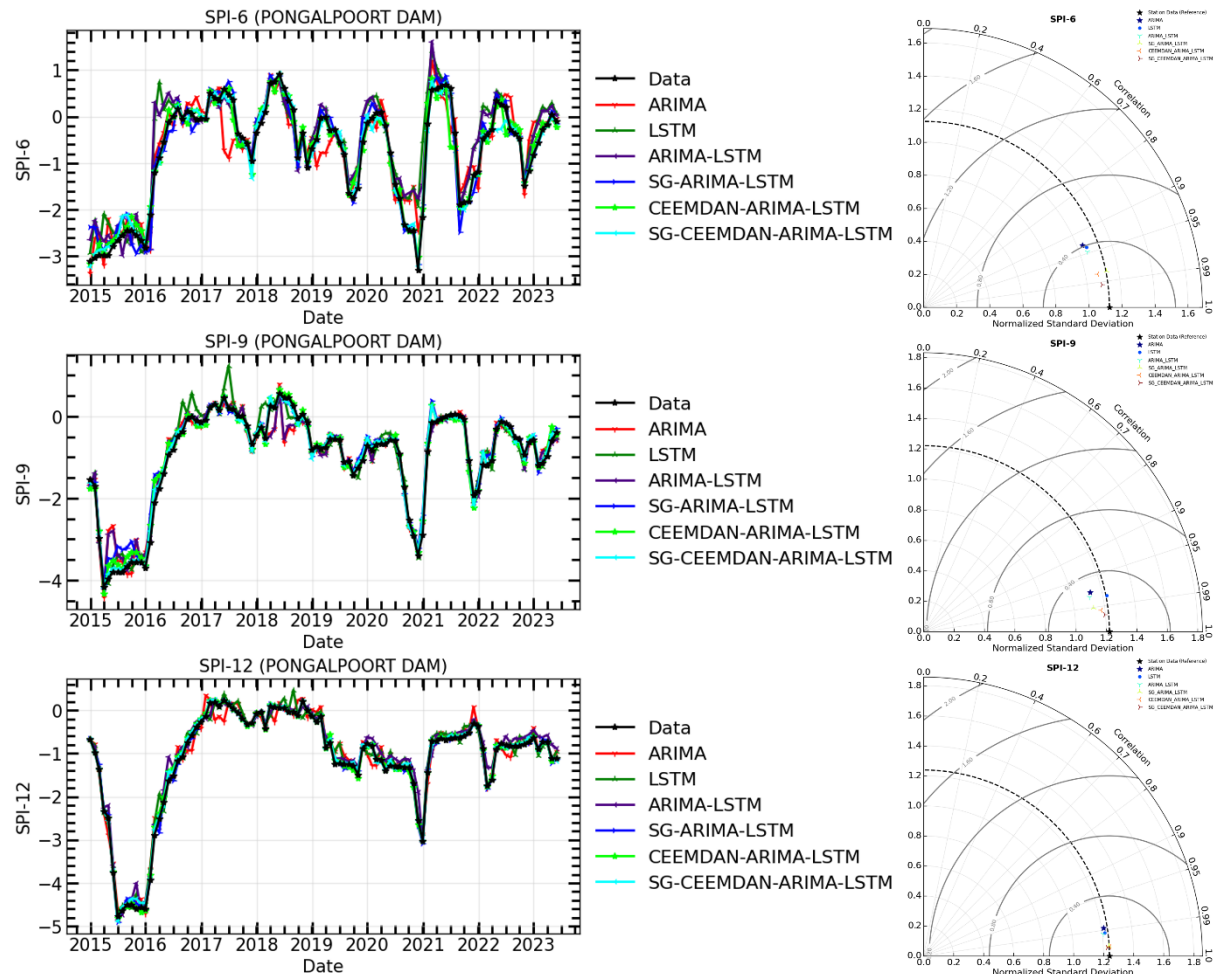
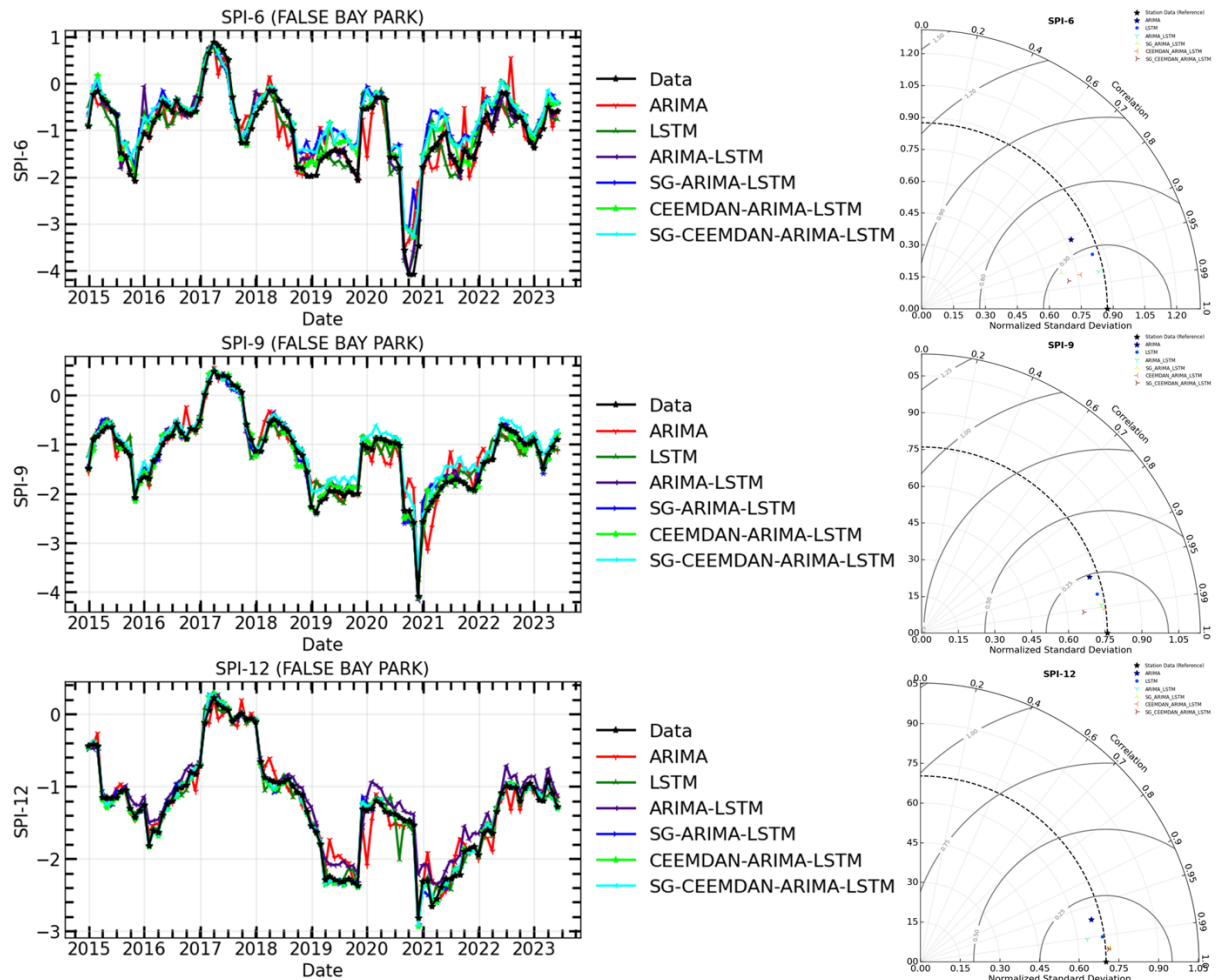


Figure 14: The time series of observations and hybrid forecasting models for SPI prediction (Left) and their Taylor diagram plots at different timescales (Right) for SPI-6, SPI-9, and SPI-12 of Mkuze Game Reserve meteorological station.



540 **Figure 15:** The time series of observations and hybrid forecasting models for SPI prediction (Left) and their Taylor diagram plots at different timescales (Right) for SPI-6, SPI-9, and SPI-12 of Pongolapoort dam meteorological station



**Figure 16: The time series of observations and hybrid forecasting models for SPI prediction (Left) and their Taylor diagram plots at different timescales (Right) for SPI-6, SPI-9, and SPI-12 of False Bay Park meteorological station.**

545

#### 4. Discussion

In this study, we utilized the Mann-Kendall and Modified Mann-Kendall tests to determine the drought trends index in meteorological variables within the basin. The MK and MMK trend methods showed a significant decrease in all SPI time scales based on rainfall data from five stations; however, the district, except for the Riverview station, showed an increasing 550 trend in the uMkhanyakude district. The study's findings align with prior research by Kganvago et al. (2021) and Ngwenya et al. (2024). Ngwenya et al. (2024) performed a study employing the Mann-Kendall test to evaluate the SPI values at a 5% significance level, revealing sustained drought conditions in the Western Cape area. Kganvago et al. (2021) indicated a notable decline in drought conditions in the Western Cape area of South Africa. We have also employed the ITA, which enhances the MK and MMK tests in identifying trends, and the results underscore the importance of comprehending drought conditions.



555 The findings of our analysis validate previous research by Naik and Abiodun (2020), highlighting the necessity of performing trend studies on drought indicators to investigate the impacts of climate change. The study underscores the essential function of SPI as a primary variable in monitoring and forecasting droughts in the region, and its potential to mitigate the detrimental impacts of droughts and water scarcity in the uMkhanyakude district in the future. The objective was to determine if the model's predictive performance is enhanced by smoothing and deconstructing time series data.

560

According to the statistical metrics in Table 4 and Taylor diagram (see Figure 11 - 16), highlight the effectiveness of hybrid models that incorporate filter and signal decomposition techniques (SG and CEEMDAN) in improving prediction accuracy, particularly for drought forecasting. These findings support other research (Taylan et al., 2021; Elbeltagi et al., 2023; Rezaiy and Shabri 2024b) highlighting the superior accuracy of hybrid drought forecasting models relative to an individual models.

565

For example, Taylan et al. (2021) developed a hybrid model to forecast drought using precipitation data from Çanakkale, Gökçeda, and Bozcaada stations between 1975 and 2010. The study found that the hybrid models, which incorporated preprocessing techniques, performed better. Elbeltagi et al. (2023) utilized a hybrid model to estimate the SPI for 3, 6, and 12-month drought periods from 2000 to 2019. The findings demonstrated that RSS-M5P model yielded the most precise SPI predictions, with  $MAE = 0.497$ ,  $RMSE = 0.682$ ,  $RAE = 81.88$ ,  $RRSE = 87.22$ , and  $R^2 = 0.507$  for SPI-3;  $MAE = 0.452$ ,

570

$RMSE = 0.717$ ,  $RAE = 69.76$ ,  $RRSE = 85.24$ , and  $R^2 = 0.402$  for SPI-6 and  $MAE = 0.294$ ,  $RMSE = 0.377$ ,  $RAE = 55.79$ ,  $RRSE = 59.57$ , and  $R^2 = 0.783$  for SPI-12. The models employed to analyse drought in Jaisalmer, Rajasthan, yielded the most effective results, exceeding those of RSS-RF and RSS-RT. Additionally, Rezaiy and Shabri (2024b) introduced a W-EEMD-ARIMA model for drought prediction. This model utilises monthly precipitation data from Kabul spanning 1970 to 2019. The  $R^2$  value was 0.9946, the MAPE was 18.9674, the RMSE was 0.0736, the MAE was 0.0575, and the SPI-12 validation indicated that our model was accurate. The outcomes obtained here surpassed those of the ARIMA, Wavelet-ARIMA, and EEMD-ARIMA models in terms of raw data (RMSE: 0.0858, MAE: 0.0660, MAPE: 24.5411,  $R^2$  : 0.9925), analytical method (MAE: 0.1874, MAPE: 60.0220,  $R^2$  : 0.9361), and maximum likelihood estimation (RMSE: 0.1002, MAE: 0.0691, MAPE: 23.7122,  $R^2$  : 0.9898). During the SPI-3, SPI-6, and SPI-9 periods, our hybrid model consistently outperformed other models.

575

Our proposed hybrid model surpasses ARIMA, Wavelet-ARIMA, and EEMD-ARIMA in enhancing the precision of drought predictions, as evidenced by this data.

580

In terms of term forecasting accuracy, the hybrid models, SG-CEEMDAN-ARIMA-LSTM in particular consistently surpassed all other models across all SPI timescales, according to a comparison of this study's results with previous research. All models successfully reproduced the original SPI time series. With the range values of RMSE of 0.1453 - 0.2314 for SPI-6, 0.0921 – 0.1631 for SPI-9, and 0.0349 – 0.07416 for SPI-12, and the highest  $R^2$  values of 0.9565 - 0.9839 for SPI-6, 0.9836 - 0.9892 for SPI-9, and 0.9939 - 0.9990 for SPI-12 across all timescales, the SG-CEEMDAN-ARIMA-LSTM model showed the most proficiency in capturing extreme values and rapid transitions. That these methods, when combined, improve the models' capacity to represent drought in uMkhanyakude district, both in the short and long term, is supported by the data. This makes



the models far better at foretelling when droughts will occur. In light of the foregoing, our study provides useful information regarding the use of the hybrid SG-CEEMDAN-ARIMA-LSTM model to the forecasting of meteorological droughts.

590

## 5. Conclusion

This study examined the trends in the Standardised Precipitation Index (SPI) over different timescales (SPI-6, SPI-9, and SPI-12) utilising the Mann-Kendall (MK), modified Mann-Kendall (MMK) test, and the innovative trend analysis (ITA) protocol. The monthly rainfall data from uMkhanyakude district, South Africa, covering the years 1980 to 2023, was used for these 595 calculations. Rainfall has been trending downward at a 95% confidence level, according to the MK and MMK tests. The ITA results supported these findings as well, revealing a declining trend with the most of data points going below the 1:1 line. In order to predict SPI data over various timescales, this research also used LSTM and autoregressive integrated moving average (ARIMA) models. Researchers used a hybrid model that combines the SG-CEEMDAN processing method with the ARIMA-LSTM model to enhance the precision of SPI forecasts. They also used SG filtering and full ensemble empirical mode 600 decomposition with adaptive noise (CEEMDAN). Figures 11–16 and Table 4 display results of a thorough comparison examination of the forecast outcomes. The results revealed that the inclusion of preprocessing techniques (SG filtering, CEEMDAN, and SG-CEEMDAN) significantly improved the model performance in forecasting SPI at all timescales. The performance consistently increased with higher timescales, potentially due to lower noise levels. Across different timescales, SG and CEEMDAN combined hybrid model consistently outperformed the individual models. Notably, the CEEMDAN-605 ARIMA-LSTM model outperformed the SG-ARIMA-LSTM model at all timescales, while the SG-CEEMDAN-ARIMA-LSTM model consistently exhibited the lowest root mean square error (RMSE) values across all indices. These results demonstrate that combining SG-CEEMDAN with ARIMA-LSTM has the potential to significantly enhance the accuracy of meteorological drought forecasting.

610 The principal conclusion of the study is that ARIMA-LSTM, in conjunction with SG, CEEMDAN, and SG-CEEMDAN, serves as an effective instrument for early warning systems and meteorological drought prediction. The proposed methodology in this paper serves as a framework for modeling complex meteorological phenomena such as drought, particularly pertinent in semi-arid regions. Enhancing model performance and creating efficient models for weather forecasting can be achieved through techniques that address data noise, nonlinearity, and nonstationarity. To enhance water resource management, make informed decisions regarding agricultural output and tourism management, and establish regulations, it is essential to acquire 615 extremely effective models for drought prediction. The omission of exogenous environmental variables in the SG-CEEMDAN-ARIMA-LSTM model represents a significant drawback of the study. The model's forecast accuracy and real-world application are limited by disregarding these exogenous effects, which can substantially affect drought conditions. Future study should aim to include external variables, including temperature, soil moisture, vegetation indices, and anthropogenic factors such as land use and water management, to improve the model's efficacy. This integration would provide a more thorough



620 comprehension of drought dynamics, hence improving the model's accuracy and dependability in drought predictions. Additionally, it is essential to investigate alternate decomposition methods, such as enhanced CEEMDAN (iCEEMDAN), which may provide significant insights.

## References

Adeola, O. M., Masinde, M., Botai, J. O., Adeola, A. M., and Botai, C. M.: An analysis of precipitation extreme events based 625 on the SPI and EDI values in the Free State Province, South Africa, *Water*, **13**, 3058, <https://doi.org/10.3390/w13213058>, 2021.

Aghelpour, P., Mohammadi, B., Mehdizadeh, S., Bahrami-Pichaghchi, H., and Duan, Z.: A novel hybrid dragonfly optimization algorithm for agricultural drought prediction, *Stoch. Environ. Res. Risk Assess.*, **35**, 2459–2477, <https://doi.org/10.1007/s00477-021-02041-0>, 2021.

630 Ahmadi, F., Mehdizadeh, S., and Mohammadi, B.: Development of bio-inspired-and wavelet-based hybrid models for reconnaissance drought index modeling, *Water Resour. Manage.*, **35**, 4127–4147, <https://doi.org/10.1007/s11269-021-02884-7>, 2021.

Alashan, S.: An improved version of innovative trend analyses, *Arab. J. Geosci.*, **11**, 50, <https://doi.org/10.1007/s12517-018-3447-4>, 2018.

635 Alashan, S.: Combination of modified Mann-Kendall method and Sen innovative trend analysis, *Eng. Rep.*, **2**, e12131, <https://doi.org/10.1002/eng2.12131>, 2020.

Alquraish, M., Abuhasel, K. A., Alqahtani, S. A., and Khadr, M.: SPI-based hybrid hidden Markov–GA, ARIMA–GA, and ARIMA–GA–ANN models for meteorological drought forecasting, *Sustainability*, **13**, 12576, <https://doi.org/10.3390/su132212576>, 2021.

640 Ashraf, M. S., Shahid, M., Waseem, M., Azam, M., and Rahman, K. U.: Assessment of variability in hydrological droughts using the improved innovative trend analysis method, *Sustain.*, **15**, 9065, <https://doi.org/10.3390/su15119065>, 2023.

Bagmar, M. S. H. and Khudri, M. M.: Application of box-jenkins models for forecasting drought in north-western part of Bangladesh, *Environmental Engineering Research*, **26**, 3, <https://doi.org/10.4491/eer.2020.607>, 2021.

Bahta, Y. T. and Myeki, V. A.: Adaptation, coping strategies and resilience of agricultural drought in South Africa: implication 645 for the sustainability of livestock sector, *Heliyon*, **7**, e08263, <https://doi.org/10.1016/j.heliyon.2021.e08263>, 2021.



Balti, H., Abbes, A. B., Mellouli, N., Farah, I. R., Sang, Y., and Lamolle, M.: A review of drought monitoring with big data: Issues, methods, challenges, and research directions, *Ecological Informatics*, **60**, 101136, <https://doi.org/10.1016/j.ecoinf.2020.101136>, 2020.

Bard, A., Renard, B., Lang, M., Giuntoli, I., Korck, J., Koboltschnig, G., ... and Volken, D.: Trends in the hydrologic regime  
650 of Alpine rivers, *J. Hydrol.*, **529**, 1823–1837, <https://doi.org/10.1016/j.jhydrol.2015.08.052>, 2015.

Bari Abarghouei, H., Asadi Zarch, M. A., Dastorani, M. T., Kousari, M. R., and Safari Zarch, M.: The survey of climatic drought trend in Iran, *Stoch. Environ. Res. Risk Assess.*, **25**, 851–863, <https://doi.org/10.1007/s00477-010-0452-0>, 2011.

Bari Abarghouei, H., Asadi Zarch, M. A., Dastorani, M. T., Kousari, M. R., and Safari Zarch, M.: The survey of climatic drought trend in Iran, *Stoch. Environ. Res. Risk Assess.*, **25**, 851–863, <https://doi.org/10.1007/s00477-010-0452-2>, 2011.

655 Baudoin, M.-A., Vogel, C., Nortje, K., and Naik, M.: Living with drought in South Africa: lessons learnt from the recent El Niño drought period, *International Journal of Disaster Risk Reduction*, **23**, 128–137, <https://doi.org/10.1016/j.ijdrr.2017.05.005>, 2017.

Box, G. E., Jenkins, G. M., Reinsel, G. C., and Ljung, G. M.: Time series analysis: forecasting and control, 5th Edn., John Wiley & Sons, Hoboken, NJ, 2015.

660 Bukhosini, Z. and Moyo, I.: An analysis of the challenges faced by small-scale farmers and their response to the 2014–2016 drought in Mfekayi, Mtubatuba, KZN, South Africa, *Afr. J. Dev. Stud.*, **13**, 1, 2023.

Caloiero, T., Coscarelli, R., Ferrari, E., and Mancini, M.: Trend detection of annual and seasonal rainfall in Calabria (Southern Italy), *Int. J. Climatol.*, **31**, 44–56, <https://doi.org/10.1002/joc.2054>, 2011.

665 Caloiero, T.: SPI trend analysis of New Zealand applying the ITA technique, *Geosci.*, **8**, 101, <https://doi.org/10.3390/geosciences8030101>, 2018.

Calverley, C. M. and Walther, S. C.: Drought, water management, and social equity: Analyzing Cape Town, South Africa's water crisis, *Front. Water*, **4**, 910149, <https://doi.org/10.3389/frwa.2022.910149>, 2022.

Chattopadhyay, S. and Edwards, D. R.: Long-term trend analysis of precipitation and air temperature for Kentucky, United States, *Climate*, **4**, 10, <https://doi.org/10.3390/cli4010010>, 2016.



670 Chen, L., He, Z., Gu, X., Xu, M., Pan, S., Tan, H., and Yang, S.: Construction of an agricultural drought monitoring model for Karst with coupled climate and substratum factors—A case study of Guizhou Province, China, *Water*, **15**, 1795, <https://doi.org/10.3390/w15091795>, 2023.

Chen, Z., Wang, G., Wei, X., Liu, Y., Duan, Z., Hu, Y., and Jiang, H.: Basin-scale daily drought prediction using convolutional neural networks in Fenhe River Basin, China, *Atmosphere*, **15**, 155, <https://doi.org/10.3390/atmos15020155>, 2024.

675 Chivangulula, F. M., Amraoui, M., and Pereira, M. G.: The drought regime in Southern Africa: A systematic review, *Climate*, **11**, 147, <https://doi.org/10.3390/cli11070147>, 2023.

Cunha, A. P. M., Zeri, M., Deusdará Leal, K., Costa, L., Cuartas, L. A., Marengo, J. A., and Ribeiro-Neto, G.: Extreme drought events over Brazil from 2011 to 2019, *Atmosphere*, **10**, 642, <https://doi.org/10.3390/atmos10110642>, 2019.

680 Danandeh Mehr, A., Sorman, A. U., Kahya, E., and Hesami Afshar, M.: Climate change impacts on meteorological drought using SPI and SPEI: case study of Ankara, Turkey, *Hydrol. Sci. J.*, **65**, 254–268, <https://doi.org/10.1080/02626667.2019.1700770>, 2020.

Di Nunno, F., de Marinis, G., and Granata, F.: Analysis of SPI index trend variations in the United Kingdom—A cluster-based and Bayesian ensemble algorithms approach, *J. Hydrol. Reg. Stud.*, **52**, 101717, <https://doi.org/10.1016/j.ejrh.2023.101717>, 2024.

685 Dikshit, A., Pradhan, B., Huete, A., and Park, H. J.: Spatial based drought assessment: Where are we heading? A review on the current status and future, *Science of The Total Environment*, **844**, 157239, <https://doi.org/10.1016/j.scitotenv.2022.157239>, 2022.

690 Ding, Y., Yu, G., Tian, R., and Sun, Y.: Application of a hybrid CEEMD-LSTM model based on the standardized precipitation index for drought forecasting: the case of the Xinjiang Uygur Autonomous Region, China, *Atmosphere*, **13**, 1504, <https://doi.org/10.3390/atmos13091504>, 2022.

Elbeltagi, A., Kumar, M., Kushwaha, N. L., Pande, C. B., Ditthakit, P., Vishwakarma, D. K., and Subeesh, A.: Drought indicator analysis and forecasting using data driven models: case study in Jaisalmer, India, *Stoch. Environ. Res. Risk Assess.*, **37**, 113–131, <https://doi.org/10.1007/s00477-022-02249-z>, 2023.

695 Farr, T. G., Rosen, P. A., Caro, E., Crippen, R., Duren, R., Hensley, S., Kobrick, M., Paller, M., Rodriguez, E., Roth, L., Seal, D., Shaffer, S., Shimada, J., Umland, J., Werner, M., Oskin, M., Burbank, D., and Alsdorf, D.: The Shuttle Radar Topography Mission, *Rev. Geophys.*, **45**, RG2004, <https://doi.org/10.1029/2005RG000183>, 2007.



Gavahi, K., Abbaszadeh, P., and Moradkhani, H.: How does precipitation data influence the land surface data assimilation for drought monitoring?, *Science of the Total Environment*, **831**, 154916, <https://doi.org/10.1016/j.scitotenv.2022.154916>, 2022.

700 Ghozat, A., Sharafati, A., Haji Seyed Asadollah, S. B., and Motta, D.: A novel intelligent approach for predicting meteorological drought based on satellite-based precipitation product: Application of an EMD-DFA-DBN hybrid model, *Computers and Electronics in Agriculture*, **211**, 107946, <https://doi.org/10.1016/j.compag.2023.107946>, 2023.

Gond, S., Gupta, N., Patel, J., and Dikshit, P. K. S.: Spatiotemporal evaluation of drought characteristics based on standard drought indices at various timescales over Uttar Pradesh, India, *Environ. Monit. Assess.*, **195**, 439, <https://doi.org/10.1007/s10661-023-11368-6>, 2023.

705 Hamed, K. H. and Rao, A. R.: A modified Mann-Kendall trend test for autocorrelated data, *J. Hydrol.*, **204**, 182–196, [https://doi.org/10.1016/S0022-1694\(97\)00125-X](https://doi.org/10.1016/S0022-1694(97)00125-X), 1998.

Harka, A. E., Jilo, N. B., and Behulu, F.: Spatial-temporal rainfall trend and variability assessment in the Upper Wabe Shebelle River Basin, Ethiopia: Application of innovative trend analysis method, *J. Hydrol. Reg. Stud.*, **37**, 100915, <https://doi.org/10.1016/j.ejrh.2021.100915>, 2021.

710 Helsel, D. R. and Hirsch, R. M.: Statistical methods in water resources, Elsevier, Amsterdam, 1993.

Hinge, G., Piplodiy, J., Sharma, A., Hamouda, M. A., and Mohamed, M. M.: Evaluation of hybrid wavelet models for regional drought forecasting, *Remote Sensing*, **14**, 6381, <https://doi.org/10.3390/rs14246381>, 2022.

715 Hirca, T., Eryilmaz Türkkan, G., and Niazkar, M.: Applications of innovative polygonal trend analyses to precipitation series of Eastern Black Sea Basin, Turkey, *Theor. Appl. Climatol.*, **147**, 651–667, <https://doi.org/10.1007/s00704-021-03856-3>, 2022.

Hochreiter, S. and Schmidhuber, J.: Long short-term memory, *Neural Comput.*, **9**, 1735–1780, <https://doi.org/10.1162/neco.1997.9.8.1735>, 1997.

720 Jehanzaib, M., Yoo, J., Kwon, H. H., and Kim, T. W.: Reassessing the frequency and severity of meteorological drought considering non-stationarity and copula-based bivariate probability, *Journal of Hydrology*, **603**, 126948, <https://doi.org/10.1016/j.jhydrol.2021.126948>, 2021.

Kalisa, W., Zhang, J., Igbawua, T., Kayiranga, A., Ujoh, F., Aondoakaa, I. S., and Nibagwire, D.: Spatial multi-criterion decision making (SMDM) drought assessment and sustainability over East Africa from 1982 to 2015, *Remote Sensing*, **13**, 5067, <https://doi.org/10.3390/rs13245067>, 2021.



Karamouz, M., Rasouli, K., and Nazif, S.: Development of a hybrid index for drought prediction: case study, *J. Hydrol. Eng.*, 725 **14**, 617–627, [https://doi.org/10.1061/\(ASCE\)HE.1943-5584.0000024](https://doi.org/10.1061/(ASCE)HE.1943-5584.0000024), 2009.

Karbasi, M., Karbasi, M., Jamei, M., Malik, A., and Azamathulla, H. M.: Development of a new wavelet-based hybrid model to forecast multi-scalar SPEI drought index (case study: Zanjan city, Iran), *Theor. Appl. Climatol.*, **147**, 499–522, <https://doi.org/10.1007/s00704-021-03779-1>, 2022.

Katipoğlu, O. M., Acar, R., Şenocak, S., and Şengül, S.: Assessment of meteorological drought trends in the Euphrates Basin, 730 Turkey, *Arab. J. Geosci.*, **15**, 555, <https://doi.org/10.1007/s12517-022-09994-4>, 2022.

Kganvago, M., Mukhawana, M. B., Mashalane, M., Mgabisa, A., and Moloele, S.: Recent trends of drought using remotely sensed and in-situ indices: Towards an integrated drought monitoring system for South Africa, in: *2021 IEEE International Geoscience and Remote Sensing Symposium IGARSS*, 6225–6228, <https://doi.org/10.1109/IGARSS47720.2021.9553994>, 2021.

735 Labudová, L., Labuda, M., and Takáč, J.: Comparison of SPI and SPEI applicability for drought impact assessment on crop production in the Danubian Lowland and the East Slovakian Lowland, *Theor. Appl. Climatol.*, **128**, 491–506, <https://doi.org/10.1007/s00704-015-1716-9>, 2017.

Latifoğlu, L. and Özger, M.: A novel approach for high-performance estimation of SPI data in drought prediction, *Sustainability*, **15**, 14046, <https://doi.org/10.3390/su151914046>, 2023.

740 Likinaw, A., Alemayehu, A., and Bewket, W.: Trends in extreme precipitation indices in Northwest Ethiopia: Comparative analysis using the Mann–Kendall and innovative trend analysis methods, *Climate*, **11**, 164, <https://doi.org/10.3390/cli11080164>, 2023.

Lloyd-Hughes, B. and Saunders, M. A.: A drought climatology for Europe, *Int. J. Climatol.*, **22**, 1571–1592, <https://doi.org/10.1002/joc.846>, 2002.

745 Ma, X., He, Y., Xu, J., van Noordwijk, M., and Lu, X.: Spatial and temporal variation in rainfall erosivity in a Himalayan watershed, *Catena*, **121**, 248–259, <https://doi.org/10.1016/j.catena.2014.05.012>, 2014.

Mann, H. B.: Nonparametric tests against trend, *Econometrica*, **13**, 245–259, <https://doi.org/10.2307/1907187>, 1945.

Marengo, J. A., Torres, R. R., and Alves, L. M.: Drought in Northeast Brazil—past, present, and future, *Theoretical and Applied Climatology*, **129**, 1189–1200, <https://doi.org/10.1007/s00704-016-1840-8>, 2017.



750 Mathivha, F. I., Mabala, L., Matimolane, S., and Mbatha, N.: El Niño-induced drought impacts on reservoir water resources in South Africa, *Atmosphere*, **15**, 249, <https://doi.org/10.3390/atmos15030249>, 2024.

McKee, T. B., Doesken, N. J., and Kleist, J.: Drought monitoring with multiple time scales, in: *Proceedings of the Conference on Applied Climatology*, Boston, MA, USA, American Meteorological Society, 1995.

McKee, T. B., Doesken, N. J., and Kleist, J.: The relationship of drought frequency and duration to time scales, in: *Proceedings of the 8th Conference on Applied Climatology*, Anaheim, California, American Meteorological Society, **17(22)**, 179–183, 1993.

Millington, N. and Scheba, S.: Day zero and the infrastructures of climate change: Water governance, inequality, and infrastructural politics in Cape Town's water crisis, *Int. J. Urban Reg. Res.*, **45**, 116–132, <https://doi.org/10.1111/1468-2427.12979>, 2021.

760 Mirabbasi, R., Ahmadi, F., and Jhajharia, D.: Comparison of parametric and non-parametric methods for trend identification in groundwater levels in Sirjan plain aquifer, Iran, *Hydrol. Res.*, **51**, 1455–1477, <https://doi.org/10.2166/nh.2020.157>, 2020.

Montgomery, D. C., Jennings, C. L., and Kulahci, M.: *Introduction to time series analysis and forecasting*, 2nd Edn., Wiley, Hoboken, NJ, 2015.

765 Ngwenya, M., Gidey, E., and Simatele, M. D.: Agroecological-based modeling of meteorological drought at 12-month time scale in the Western Cape Province of South Africa, *Earth Sci. Inform.*, **17**, 1851–1865, <https://doi.org/10.1007/s12145-023-01131-7>, 2024.

Olagunju, A., Thondhlana, G., Chilima, J. S., Sène-Harper, A., Compaoré, W. N., and Ohiozebau, E.: Water governance research in Africa: progress, challenges and an agenda for research and action, *Water International*, **44**, 382–407, <https://doi.org/10.1080/02508060.2019.1617950>, 2019.

770 Öztopal, A. and Şen, Z.: Innovative trend methodology applications to precipitation records in Turkey, *Water Resour. Manag.*, **31**, 727–737, <https://doi.org/10.1007/s11269-016-1343-1>, 2017.

Phuong, D. N. D., Hai, L. M., Dung, H. M., and Loi, N. K.: Temporal trend possibilities of annual rainfall and standardized precipitation index in the Central Highlands, Vietnam, *Earth Syst. Environ.*, <https://doi.org/10.1007/s41748-022-00330-0>, 2022.

775 Piri, J., Abdolahipour, M., and Keshtegar, B.: Advanced machine learning model for prediction of drought indices using hybrid SVR-RSM, *Water Resour. Manag.*, **37**, 683–712, <https://doi.org/10.1007/s11269-022-03418-5>, 2023.



Polong, F., Chen, H., Sun, S., and Ongoma, V.: Temporal and spatial evolution of the standard precipitation evapotranspiration index (SPEI) in the Tana River Basin, Kenya, *Theor. Appl. Climatol.*, 138, 777–792, <https://doi.org/10.1007/s00704-019-02841-w>, 2019.

780 Rezaiy, R. and Shabri, A.: An innovative hybrid W-EEMD-ARIMA model for drought forecasting using the standardized precipitation index, *Nat. Hazards*, <https://doi.org/10.1007/s11069-024-06460-w>, 2024b.

Rezaiy, R. and Shabri, A.: Drought forecasting using W-ARIMA model with standardized precipitation index, *J. Water Clim. Change*, 14, 3345–3367, <https://doi.org/10.2166/wcc.2023.209>, 2023.

785 Rezaiy, R. and Shabri, A.: Improving drought prediction accuracy: a hybrid EEMD and support vector machine approach with standardized precipitation index, *Water Resour. Manage.*, <https://doi.org/10.1007/s11269-024-03710-2>, 2024a.

Rusca, M., Savelli, E., Di Baldassarre, G., Biza, A., and Messori, G.: Unprecedented droughts are expected to exacerbate urban inequalities in Southern Africa, *Nat. Clim. Change*, 13, 98–105, <https://doi.org/10.1038/s41558-022-01561-1>, 2023.

Ruwanza, S., Thondhlana, G., and Falayi, M.: Research progress and conceptual insights on drought impacts and responses among smallholder farmers in South Africa: a review, *Land*, 11, 159, <https://doi.org/10.3390/land11020159>, 2022.

790 Salisu, A. M. and Shabri, A.: A hybrid wavelet-ARIMA model for standardized precipitation index drought forecasting, *Matematika*, 36, 141–156, <https://doi.org/10.11113/matematika.v36.n1.1025>, 2020.

Savitzky, A. and Golay, M. J. E.: Smoothing and differentiation of data by simplified least squares procedures, *Anal. Chem.*, 36, 1627–1639, <https://doi.org/10.1021/ac60214a047>, 1964.

795 Şen, Z.: Innovative trend analysis methodology, *J. Hydrol. Eng.*, 17, 1042–1046, [https://doi.org/10.1061/\(ASCE\)HE.1943-5584.0000556](https://doi.org/10.1061/(ASCE)HE.1943-5584.0000556), 2012.

Şen, Z.: Innovative trend significance test and applications, *Theor. Appl. Climatol.*, 127, 939–947, <https://doi.org/10.1007/s00704-015-1658-2>, 2017.

Shang, J., Zhao, B., Hua, H., Wei, J., Qin, G., and Chen, G.: Application of Informer Model Based on SPEI for Drought Forecasting, *Atmosphere*, 14, 951, <https://doi.org/10.3390/atmos14060951>, 2023.

800 Sharifi, A., Baubekova, A., Patro, E. R., Klöve, B., and Haghghi, A. T.: The combined effects of anthropogenic and climate change on river flow alterations in the Southern Caspian Sea, Iran, *Heliyon*, 10, e18663, <https://doi.org/10.1016/j.heliyon.2024.e18663>, 2024.



Shiferaw, B., Tesfaye, K., Kassie, M., Abate, T., Prasanna, B. M., and Menkir, A.: Managing vulnerability to drought and enhancing livelihood resilience in sub-Saharan Africa: Technological, institutional and policy options, *Weather and Climate Extremes*, **3**, 67–79, <https://doi.org/10.1016/j.wace.2014.03.001>, 2014.

805 Shiru, M. S., Shahid, S., Alias, N., and Chung, E. S.: Trend analysis of droughts during crop growing seasons of Nigeria, *Sustainability*, **10**, 871, <https://doi.org/10.3390/su10030871>, 2018.

Sibiya, S., Mbatha, N., Ramroop, S., Melesse, S., and Silwimba, F.: Forecasting of Standardized Precipitation Index Using Hybrid Models: A Case Study of Cape Town, South Africa, *Water*, **16**, 2469, <https://doi.org/10.3390/w16172469>, 2024.

810 Song, Y. and Park, M.: A study on the appropriateness of the drought index estimation method using damage data from Gyeongsangnamdo, South Korea, *Atmosphere*, **12**, 998, <https://doi.org/10.3390/atmos12080998>, 2021.

Sousa, P. M., Blamey, R. C., Reason, C. J. C., Ramos, A. M., and Trigo, R. M.: The ‘Day Zero’ Cape Town drought and the poleward migration of moisture corridors, *Environmental Research Letters*, **13**, 124025, <https://doi.org/10.1088/1748-9326/aae9f6>, 2018.

815 Tan, Y. X., Ng, J. L., and Huang, Y. F.: A review on drought index forecasting and their modelling approaches, *Archives of Computational Methods in Engineering*, **30**, 1111–1129, <https://doi.org/10.1007/s11831-022-09738-8>, 2023.

Taylor, K. E.: Summarizing multiple aspects of model performance in a single diagram, *J. Geophys. Res.-Atmos.*, **106**, 7183–7192, <https://doi.org/10.1029/2000JD900719>, 2001.

820 Wang, X., Hou, X., and Wang, Y.: Spatiotemporal variations and regional differences of extreme precipitation events in the coastal area of China from 1961 to 2014, *Atmos. Res.*, **197**, 94–104, <https://doi.org/10.1016/j.atmosres.2017.06.010>, 2017.

Wilhite, D. A. and Glantz, M. H.: Understanding: the drought phenomenon: the role of definitions, *Water International*, **10**, 111–120, <https://doi.org/10.1080/02508068508686328>, 1985.

825 Xu, D., Ding, Y., Liu, H., Zhang, Q., and Zhang, D.: Applicability of a CEEMD–ARIMA combined model for drought forecasting: a case study in the Ningxia Hui Autonomous Region, *Atmosphere*, **13**, 1109, <https://doi.org/10.3390/atmos13071109>, 2022.

Xu, D., Zhang, Q., Ding, Y., and Zhang, D.: Application of a hybrid ARIMA-LSTM model based on the SPEI for drought forecasting, *Environmental Science and Pollution Research*, **29**, 4128–4144, <https://doi.org/10.1007/s11356-021-15618-4>, 2022.



Yang, M., Yan, D., Yu, Y., and Yang, Z.: SPEI-based spatiotemporal analysis of drought in Haihe River Basin from 1961 to  
830 2010, *Adv. Meteorol.*, 2016, 7658015, <https://doi.org/10.1155/2016/7658015>, 2016.

Yue, S., Pilon, P., Phinney, B., and Cavadias, G.: The influence of autocorrelation on the ability to detect trend in hydrological series, *Hydrol. Process.*, 16, 1807–1829, <https://doi.org/10.1002/hyp.1095>, 2002.

Zena Besha, K., Demissie, T. A., and Feyessa, F. F.: Comparative analysis of long-term precipitation trends and its implication in the Modjo catchment, central Ethiopia, *J. Water Clim. Change*, 13, 3883–3905, <https://doi.org/10.2166/wcc.2022.089>, 2022.

835 Zhang, G. P.: Time series forecasting using a hybrid ARIMA and neural network model, *Neurocomputing*, 50, 159–175, [https://doi.org/10.1016/S0925-2312\(01\)00702-0](https://doi.org/10.1016/S0925-2312(01)00702-0), 2003.

Zhang, H., Loaiciga, H. A., and Sauter, T.: A novel fusion-based methodology for drought forecasting, *Remote Sensing*, 16, 828, <https://doi.org/10.3390/rs16050828>, 2024.

840 Zhang, X., Duan, Y., Duan, J., Chen, L., Jian, D., Lv, M., and Ma, Z.: A daily drought index-based regional drought forecasting using the Global Forecast System model outputs over China, *Atmospheric Research*, 273, 106166, <https://doi.org/10.1016/j.atmosres.2022.106166>, 2022.

Zhang, X., Qiao, W., Huang, J., Shi, J., and Zhang, M.: Flow prediction in the lower Yellow River based on CEEMDAN-BILSTM coupled model, *Water Supply*, 23, 396–409, <https://doi.org/10.2166/ws.2022.215>, 2023.

845 Zuo, D., Hou, W., Wu, H., Yan, P., and Zhang, Q.: Feasibility of calculating standardized precipitation index with short-term precipitation data in China, *Atmosphere*, 12, 603, <https://doi.org/10.3390/atmos12050603>, 2021.